Strangeness Enhancement in Heavy Ion Collisions at the WA97 Experiment

G. Torrieri

October 1999

0.1 Acknowledgements

Had I not existed, this report would not have been written. Likewise had I not learned to be curious about the world and the value of learning, the possibility that I would come to do what I do would be very small indeed. My first and foremost thank you, therefore, goes to Mum and Dad.

Then it's impossible not to mention my supervisors Orlando Villalobos-Baillie , David Evans and John Kinson, who ,though super-human patience at my incessant questions and lack of understanding of the most elementary concepts, managed to guide me through the meanders of beginner's particle physics research Let's just hope the end result of my activities will make them happy to have their name associated with it.

0.2 Author's contribution

The author wrote and tested the primary vertex finding programs for both primary negatively charged particles and the V^0 s, using both numerical and analytical algorithms. Also, the author performed the complete analysis of negative events, from the selection of reliable events to the estimation of total numbers of events and the calculation of inverse slopes and yields. Finally, a basic beam reconstruction efficiency calculation was performed. Other procedures mentioned in the thesis, such as event selection for hyperons or beam misalignement, were repeated and checked. The author participated in the online data-taking during all experiment runs in 1997 and 1998.

Contents

List of Tables

List of Figures

Chapter 1

The Strong Interaction and Quark-Gluon Plasma (QGP)

1.1 Introduction

The purpose of this investigation is to observe the behaviour of strongly interacting systems at extreme conditions of temperature and pressure, conditions that existed up to 10^{-5} seconds after the Big Bang.

The current theory that describes strong interactions predicts that, given that baryon temperature and pressure are high enough, the baryons themselves will "melt", with their constituents forming a new state of matter (analogous to the electron-nucleus- photon plasma which forms at a temperature too high to keep atoms together). Heavy ion collision experiments aim to produce such a state of matter and study its properties.

1.2 Quantum chromodynamics (QCD)

Quantum chromodynamics has been developed to describe the behaviour of the strong interaction, responsible for the binding of hadrons and nuclei. It assumes that hadrons are composed of elementary objects called "Quarks", carrying a charge called colour. Interquark interactions are mediated by spin-1 bosons, called gluons. As QED, QCD is a relativistic quantum field theory, arising from the requirement that the strong interaction Lagrangian obeys a certain symmetry (In the QCD case, it is the invariance under the SU(3) group, composed of transformations of the type

$e^{\sum_{i=1}^{8} \alpha_i T^i}$ where T^i are the set of Gell-Man 3×3 matrices and α_i are 8 arbitrary real numbers).

However, QCD presents several differences with respect to QED, which can explain the remarkable properties of hadronic matter, such as confinement. The main differences are that:

- in QCD 3 colours (commonly called "red", "green" and "blue"), and the corresponding "anti-colours" are possible. A neutral object can be formed either by binding a colour with it's respective anti-colour or by a combination of the three colours (or the three anticolours). In the quark model, mesons are bound states of a quark and an antiquark and baryons are 3-quark bound states.
- SU(3), unlike QED's generating group U(1), is non-abelian. This gives rise to interaction terms which are cubic and quartic in the colour field. In other words, gluons themselves carry colour charge and gluon-gluon couplings as those shown in Fig. 1.1, are possible.

As a consequence, gluon only loops are possible, while QED higher level diagrams need to involve an electron-positron loop as shown in Fig. 1.2. As gluons are massless, these corrections do not have a low-energy cut-off (Unlike the QED electron-positron corrections), and the QCD coupling constant is low-momentum (infrared) divergent. For this reason, perturbative calculations are only possible in a high momentum regime (such as deep inelastic scattering

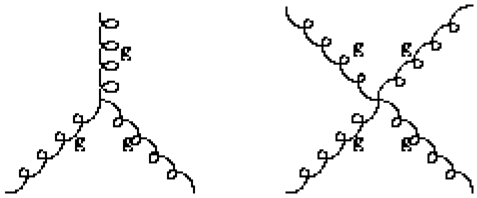

Figure 1.1: Examples of gluon-gluon vertices allowed in QCD

experiments), and obtaining numerical predictions at the low-energy (ie baryon binding energy) scale is only possible through numerical calculations.

1.3 Confinement

Because of the difficulty in doing low-energy computations, a number of phenomenological models have been developed to account for the main properties of hadronic matter. Perhaps the most important of such properties is confinement: It has been experimentally observed that quarks and gluons, while behaving like free particles at small distances (the Heisenberg "equivalent" to high momentum transfers), will exhibit an infinite binding energy when the distance scale increases.

One way to model this behaviour using QCD is to assume that the colour field lines, in a vacuum, will attract each-other, and hence the field between two quarks will be squeezed into a "tight string" running between the two quarks. The tension of such a string will contribute to the forces between quarks, giving rise to a "string tension" component proportional to distance in the QCD potential, alongside the more familiar "Coloumb" attraction component:

$$V(r) = \frac{\alpha_s}{r} + \gamma r \tag{1.1}$$

An alternative way to visualise this is via an anti-screening effect provided by QCD gluon-only loops: As in the QED-charge case, radiative corrections will lead to an "effective charge" different from the "bare charge" of the particle. However, in contrast to QED, the effective charge due to gluon-loop corrections will be higher than the bare charge.

The phenomenological model of a hadron, in such a picture, is that of a bag with finite volume V in which all colour field is expelled. Inside the bag, the quarks and gluons will behave as free particles, but extracting a quark from the bag into the "true" QCD vacuum will give rise to the formation of colour field strings and higher effective charges. Because of the string potential, having a free quark outside the bag would require infinite energy.

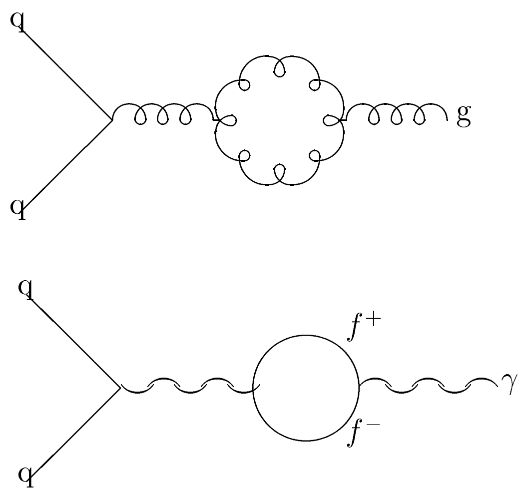

Figure 1.2: Above: QCD (anti-screening) gluon loop correction Below: QED e^+e^- loop (screening) correction.

1.4 Quark-Gluon Plasma (QGP)

If separating hadrons into constituent quarks is impossible, it turns out that QCD allows the "next-best thing".

At a sufficiently high temperature (170 MeV [1]) T_c, because of the decrease in α_s, the colour field within a hadron becomes comparable to the residual colour field coming from neighbouring hadrons. At this point a phase transition occurs within the system, individual hadrons melt away and quarks and gluons become quasi-free particles in a large hadronic system: a Quark-Gluon Plasma (QGP). (In the bag model this is equivalent to the bags of each individual hadron melting into one large bag)

To create such a plasma under laboratory conditions, a large number of hadrons must be compressed together to achieve a sufficiently high temperature and density. Making two heavy ions collide at high energy is the most simple way to achieve this. Fig. 1.3 shows a phase diagram of hadronic matter and a progression the fireball of such a collision would follow through it.

Producing and studying a QGP would present us with many scientific rewards:

First of all, it is a test of QCD's predictions, as well as an opportunity to study a QCD non-perturbative system.

Moreover, the QGP phase transition is the only one accessible to any particle physics experiments conceivable today (the energy scale of other transitions, such as Electroweak symmetry restoration, is higher by several orders of magnitude). To observe such phase transition, and the subsequent "freeze-out" and re-hadronisation as temperature decreases, is a test of quantum field theory in general.

In addition, a QGP is a mainly strongly-interacting system which is large enough to be studied from a thermodynamical/statistical prospective. A detailed analysis of it would, for instance, enable us to draw the phase diagram for strongly-interacting systems or see changes of entropy as hadronic systems change their form. As other particle physics experiments tend to study systems too small for statistical mechanics terms to have meaning (at most, proton-proton collisions of little more than 6 interacting constituents) creating a QGP is a unique opportunity for high-energy physics in general.

Finally, the QGP is interesting from a cosmological and astrophysical perspective: It is thought that the universe was a QGP up to 10^{-5} seconds after the Big Bang. It is also postulated that a QGP exists in the core of neutron stars. (See Fig. 1.3)

There seems, therefore, to be a strong incentive for producing and analysing QGP in laboratory conditions. The main problem, however, is that one cannot observe it *directly*, but must infer its existence and characteristics from what comes out after the QGP has hadronised.

1.5 Some QGP Signatures

A number of QGP signatures have been proposed, and there is considerable controversy as to their effectiveness. This section gives an overview of them and the experimental results they gave so far.

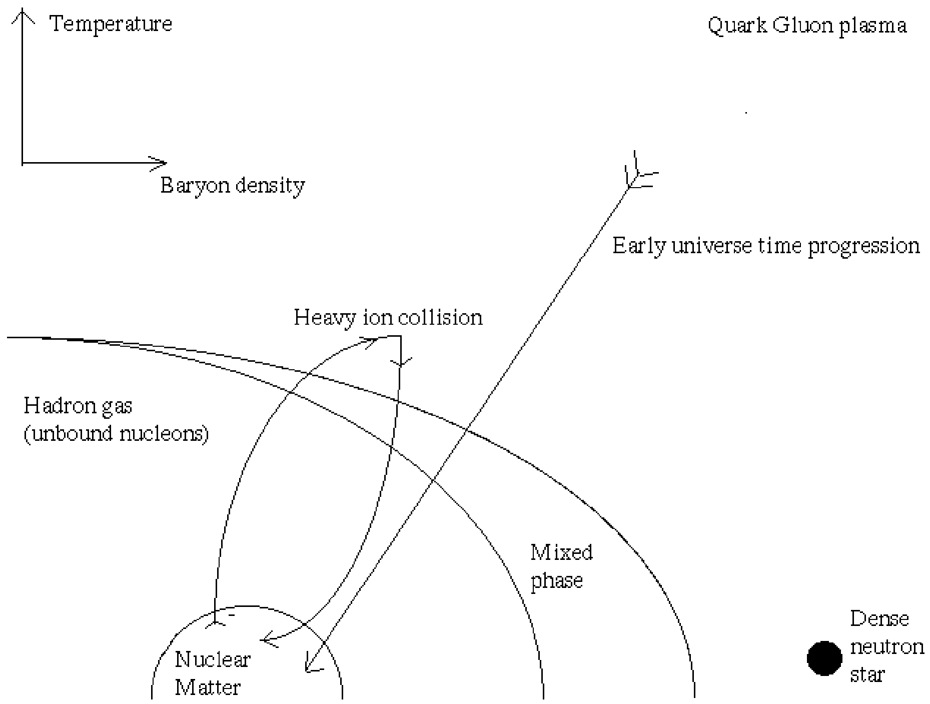

Figure 1.3: The expected phase diagram for hadronic matter, together with the positions on it of a heavy ion collision, the expanding universe and a neutron star

1.5.1 Global Variables

The most direct approach would be to try to detect a modification in the equation of state, corresponding to a sudden increase in the number of degrees of freedom of the system as it becomes a QGP. It is possible to correlate the parameters of the equation of state with observables (customarily the temperature T and the energy density ϵ are correlated to the transverse momentum p_T and dN/dy, where N is the hadron multiplicity and y the rapidity), so extensive investigations in this respect are planned in future experiments (ALICE and RHIC) at very high energy.

However, numerical simulations suggest that such a QGP signature would be weak and hence difficult to detect. In addition, the final-state observables will not only depend on the QGP phase, but on all the phases the system goes through between the collision and hadronisation (see Fig. 1.3); Therefore any such signal will be extremely ambigous and difficult to interpret, especially at lower energies where there will only be a "partial" phase transition to the mixed phase [3]. It is therefore desirable to look for a more indirect signature of a phase transition. A short description of the most promising is provided below.

1.5.2 Charmonium suppression

It has been shown that above a certain temperature ($> T_c$, where the exact temperature depends on the particular Charmonium system) the $c\overline{c}$ bound state cannot be maintained. The c$\overline{c}$ system is considerably larger that the mean distance between quarks and gluons in a QGP, so the 2 quarks become separated by colour screening. Hence, a suppression of the J/Ψ or Ψ' would be an indicator of a phase transition in which the baryon density has increased. The main feature of this signature is that it is a direct way to probe the early stages of the collision, and is completely unaffected by the freeze-out and hadronisation of the fireball. As well as detecting a phase transition, such a method can probe the state of the hadronic matter by measuring the extent of the suppression of the different $c\overline{c}$ states. J/Ψ or Ψ' are detected by their decays into muon pairs, and the main background to these events is provided by Drell-Yan processes. Fig. 1.4 [5]

This approach has been tried, and J/Ψ suppression observed, by the NA38 (O and S ion collisions) [6] and NA50 (heavier Pb-Pb collisions) experiments.

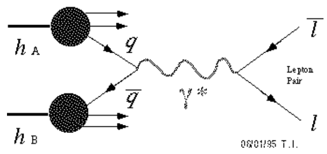

Figure 1.4: Drell-Yan process: 2 quarks from 2 different hadrons annihilate to produce a dimuon pair

However,

- The J/Ψ may survive if it escapes the high-density region, which is possible if it has enough p_T or if the QGP cools down very fast. Hence, the signature is weakened
- Charmonium suppression processes are expected in a hadron gas, as J/Ψ has a large (6 mb) interaction cross-section in nuclear matter.

Hence, NA38 results cannot be attributed unambiguously to the QGP mechanism. More recent NA50 results [7] Fig. 1.5, however, show a suppression which can only be explained with great difficulty by non-QGP mechanisms. These results, together with strangeness enhancement, are a strong indication that QGP has already been produced.

1.5.3 Direct photon production

This method relies on the production of photons in a QGP by the process illustrated in Fig. 1.6

However, there are large backgrounds due to electromagnetic decays in pseudoscalar mesons (eg the π^0) [1]. In addition, hadron gas also allows many direct-photon producing processes, such as the $\pi\rho \rightarrow \gamma\rho$. According to modern simulations both the direct photon intensity and energy distribution of QGP close to T_c is roughly equal to that of the hadron gas. [2]

At $T >> T_c$ QGP-related direct photons (especially at high p_T) should be dominant, something the ALICE Photon spectrometer will be able to measure [11].

1.5.4 Lepton pairs

A measurement of the yield of lepton pairs in a heavy ion collision, can test the state of hadronic matter in two distinct ways. As shown in Fig. 1.7, lepton pairs can be created in a QGP by a first order process than could happen at a much lower threshold than a baryon-baryon interaction (which involves two or more quarks). In addition, since dilepton pairs are produced in meson decays, their energy distribution can be used to detect and measure a restoration of chiral symmetry, since such a restoration will lower the meson's masses. (Chiral symmetry restoration is not trivially associated with QGP formation. However, recent lattice calculations have shown that the two transitions should coincide [8]).

The direct QGP signal has to compete with $l\bar{l}$ pairs produced in decay leptons from several resonances [2], and, at 1-1.5 GeV or more, it is superseded by nucleon-nucleon Drell-Yan processes [3]. Hence, the background for such a QGP signature is truly formidable! Despite this, lepton pair production is considered both a phase state probe and an indicator of thermalisation time for present and future experiments [10]. At present an excess of lepton pairs has been observed in Pb-Au collisions in NA45 (Fig. 1.8) at a rest frame energy of 0.4-0.6 GeV. The interpretation of this result is controversial, but the favoured explanation is that the extra leptons come from decays of ρ s, the mass of which has been shifted by partial chiral symmetry restoration [9]). A future run with the upgraded apparatus is needed to verify this interpretation. Subsequently, direct lepton pairs will be studied in the LHC ALICE detector [11].

1.5.5 Strangeness enhancement

This is the method many theorists regard as very promising. It is also the method used by the experiment described in this report. Analogously with the arguments above, creation of strange quark-antiquark pairs via annihilations of semi-free quarks such as Fig. 1.9 which occurs at a threshold of 300 MeV (lowered by a restoration of chiral symmetry) has a much lower threshold than hadronic processes of strange quark production: The easiest of those is π p $\rightarrow$ Λ K which has a threshold of 530 MeV.

In addition, the Pauli exclusion principle will provide a further boost to strange quark formation in a QGP created by heavy ion collisions, since the initial constituents will be predominantly u and d quarks. This is even more true for strange antibaryons in a gluon-rich QGP, since (unlike in the hadron gas phase) strange anti-quarks can be produced with relative ease even in the absence of initial state $\overline{u}$ and $\overline{d}$ quarks by gluonic processes shown in Fig. 1.10. The combined saturation time for these processes was calculated to be about 10^{-23} sec. at the expected phase transition temperature, comparable to the lifetime of the fireball. Thermal equilibrium as well as chemical equilibrium of gluons and light quarks is reached more quickly by an order of magnitude. Therefore, most strange quarks will be created from annihilations of components with an equilibrium momentum distribution [13].

During hadronisation, 3 antiquarks can combine into heavy strange antibaryons with relative ease. In contrast, in a hadron gas, the creation of heavy strange baryons and antibaryons is especially energetically intensive because of baryon and strangeness conservation ($pp \rightarrow pp\Lambda\overline{\Lambda}$, for example, has a threshold energy of 2.23 GeV).

Calculations show that a hot hadron gas could, in chemical equilibrium, give a strange particle yield comparable to that of a QGP. However, such a hadron gas takes a much longer (an order of magnitude longer) time to reach such an equilibrium than a QGP. This is more than the life-time of a typical fireball generated by heavy ion collisions. [14] In addition, a hadron gas's entropy and chemical potential per strangeness content will be different from a QGP, and the difference would be strong enough to be detected by a modern strangeness enhancement experiment. [16] [15]

Comparison of the number of strange baryons and anti-baryons produced in heavy ion collisions with a control system, in which QGP formation is known not to have occurred (such as proton-nucleus collisions) will therefore provide a good indicator of whether a phase transition has occurred. The next section will describe some of the more detailed analysis that can be performed.

1.5.6 Strangeness enhancement as a probe into the hadronic matter's equation of state

Assuming chemical equilibrium to have been reached within the fireball,

$\frac{dN_i}{dy} = g_i \gamma_i \lambda_i \int_{m_T^{cut}}^{\infty} m_T y e^{-m_T y/T} dm_T^2$

where

- $\lambda_i = e^{\frac{-\mu_i}{T}}$ is the fugacity
- γ_i is a factor accounting for each flavour's saturation (=1 at equilibrium and for u and d quarks)
- g_i is a factor accounting for the degeneracy

- $m_T = \sqrt{m^2 + p_T^2}$

$(c = k = 1)$

Therefore, for two different flavours i and j, the ratio

$$\frac{\frac{dN_i}{dy}}{\frac{dN_j}{dy}} = \frac{g_i \lambda_i \gamma_i}{g_j \lambda_j \gamma_j}$$

is only going to depend on the fugacities and, γ_i and g_i.

Neglecting resonance decays, assuming hadronisation to happen between uncorrelated quarks, and considering that

- $\gamma_s = \gamma_{\overline{s}}$ since s and $\overline{s}$ are created in pairs
- $\mu_q = -\mu_{\overline{q}}$, $\lambda_q = \lambda_{\overline{q}}^{-1}$, since since adding an antiquark to the system would be equivalent to annihilating a quark of the same flavour.

It follows that, within a narrow central rapidity region (such as the one examined by the WA97 experiment, see next chapter):

$$R_\Lambda = \frac{\overline{\Lambda}}{\Lambda} = (\lambda_d \lambda_u \lambda_s)^{-2}$$

$$R_\Xi = \frac{\overline{\Xi}}{\Xi} = (\lambda_d \lambda_s^2)^{-2}$$

$$R_\Omega = \frac{\overline{\Omega}}{\Omega} = \lambda_s^{-6}$$

Hence, the ratios of hyperons to anti-hyperons provides a handle to estimate the chemical potential of the system. (Neglecting resonances is a good, but not perfect approximation. If resonances are considered, the ratios will be equal to a more complicated expression containing the branching ratio and $\frac{dN}{dY}$ of the various resonances. However, as the main resonances of Λ, Ξ and Ω, have been studied, $R_{\Lambda,\Xi,\Omega}$ can still be used to obtain the fugacities). In practice, until recently no statistically significant sample of Ω s was produced in heavy ion collisions. Therefore, chemical potentials have so far been obtained by

$$R_{\Lambda} R_{\Xi}^{-2} = e^{\frac{6\mu_s}{T}} e^{\frac{2\delta\mu}{T}}$$

$$R_{\Xi} R_{\Lambda}^{-2} = e^{\frac{6\mu_q}{T}} e^{\frac{2\delta\mu}{T}}$$

where $\delta\mu$ is $\mu_u - \mu_d \simeq 0$

γ_s can also be measured from the ratio

$$\frac{\Xi^-}{\Lambda} \frac{\Xi^+}{\overline{\Lambda}} = \gamma_s^2$$

The fireball's temperature can be extracted from a fit of $\frac{dN}{dm_T} = f(y) m_T^{\alpha} e^{-\frac{m_T}{T}}$ to the m_T distribution, assuming thermal equilibrium (which is reached well before chemical equilibrium in all models) and bearing in mind that the effective temperature is modified by the transverse flow of the particles. The entropy contents of the fireball can be inferred from the particle multiplicity of the event, as the baryon and pion entropy content in a nucleon and meson gas have been calculated [17] . The crucial assumption which makes such a measurement significant is that most of the entropy is produced during the the approach to equilibrium (where a phase transition has occurred), rather than in the latter freeze-out and hadronisation. Fortunately, this has been shown to be the case [18]

1.5.7 Summary of results produced so far

The WA85 and WA94 collaborations have published the yields and enhancement, and ratios of Λ s and Ξ s in S-S collisions at 200 GeV in the region of central rapidity. WA97, operating with lead-lead ions at 160 GeV, has collected, for the first time, data on Ω production. Figures 1.11 and 1.12 show the WA97 strange particle yields plotted against the number of participants, and the enhancements as normalised to the p-Pb yield. (The enhancement is defined as $(\frac{Yield}{N_{participants}})_{Pb-Pb}/(\frac{Yield}{N_{participants}})_{p-Pb})$ As can be seen, there is a marked enhancement which goes well beyond the increase of the number of participants. Moreover, this enhancement increases with the baryon strangeness contents (so Ω s are consistently more enhanced than Ξ s, which are more enhanced than Λ s) [20]. As explained before, such results are explained much more easily by QGP-based models than by hadron gas ones [22].

Particle ratios have also been measured, and the results so far are given in table 1.1 and 1.2. The m_T distribution for each particle, from which the inverse slopes (effective temperatures) can be read, is shown in Fig. 1.13 [21]. These measurements have been used to estimate Temperature and chemical potentials of the fireball, and to fit the system to various thermal models [15]. At present, results of the measurements are consistently explained much better by QGP-based thermal models than by hadron gas based ones. In particular, the particle ratios cited in tables 1.1 and 1.2 yield a strange chemical potential very close to 0.
In a QGP, such a result is the direct consequence of the fact that the net strangeness in the fireball is 0: As in a QGP all negative strangeness is carried by quarks, while the only positive strange carrier is the strange antiquark, their equal abundancies make the total chemical potential cancel out.
This is less obvious in a hadron gas: While the net strangeness is still 0, quarks and anti-quarks might be carried by hadrons of a different mass, resulting in a

net non-zero chemical potential.

In fact, a strong tendency towards a non-zero chemical potential exists in all hadron gas models, as the lower-threshold strangeness producing reactions always result in quarks going into baryons and anti-quarks going into mesons.

By suitably changing other parameters in the hadron gas partition function, such as temperature and the phase space factors of different hadrons, it is possible to reconcile hadron gas models to a 0 strange chemical potential.

However, this looks extremely artificial compared to the natural way the chemical potential is accounted for by the QGP model.

In this context, a measurement which would help to distinguish between the two models is an entropy measurement together with a strangeness enhancement measurement: The temperature and chemical potential of the hadron gas model consistent with the observed strangeness yields would produce an entropy lower by an order of magnitude to the QGP model. This is more than sensitive enough for today's experiments [15].

The near equality of inverse slopes is also accounted for more naturally by QGP: If the hyperons are the result of a quickly hadronised QGP fireball, one would indeed expect the similar temperatures and flow velocities for different hyperons. This is a lot less obvious if the hyperons came from a hadron gas, let alone one which probably did not reach equilibrium. Again, by adjusting the freeze-out times for each hyperon appropriately, the hadron gas scenario can account for the observed parameters, but with considerably less ease. [19].

In conclusion, while the QGP model is considerably better at explaining the observed results, non-QGP mechanisms still cannot be excluded. Further measurements and analysis, therefore, is still needed. This thesis will describe the completion of the analysis of WA97 data, and introduce further experiments in the field.

Table 1.1: Ratios of Ξ and Λ particles from the WA97 and WA94 experiments.

	WA97 (Pb-Pb)	WA94 (S-S)
$\frac{\Xi^-}{\Lambda}$	0.14 ± 0.02	0.09 ± 0.01
$\frac{\overline{\Xi}^+}{\overline{\Lambda}}$	0.29 ± 0.05	0.21 ± 0.02
$\frac{\overline{\Lambda}}{\Lambda}$	0.13 ± 0.02	0.22 ± 0.01
$\frac{\overline{\Xi}^+}{\Xi^-}$	0.27 ± 0.05	0.55 ± 0.07

Table 1.2: Ratios of Ω and Ξ particles from the WA97 experiment.

	WA97 results (Pb-Pb)
$\frac{\Omega^-}{\Xi^-}$	0.19 ± 0.04
$\frac{\overline{\Omega}^+}{\overline{\Xi}^+}$	0.30 ± 0.09
$\frac{\overline{\Omega}^+}{\Omega^-}$	0.42 ± 0.12

1.5.8 Objectives of the analysis described in this report

In the WA97 data analysed so far, p-Nucleus collisions have been used as control events. More recently, WA97 has done additional runs with proton-beryllium collisions. Since these are considerably more symmetrical than p-nucleus events, they are much better suited as control events for symmetrical heavy ion collisions such as Pb-Pb. The subsequent chapters will describe in detail some of the analysis performed on these p-Be events.

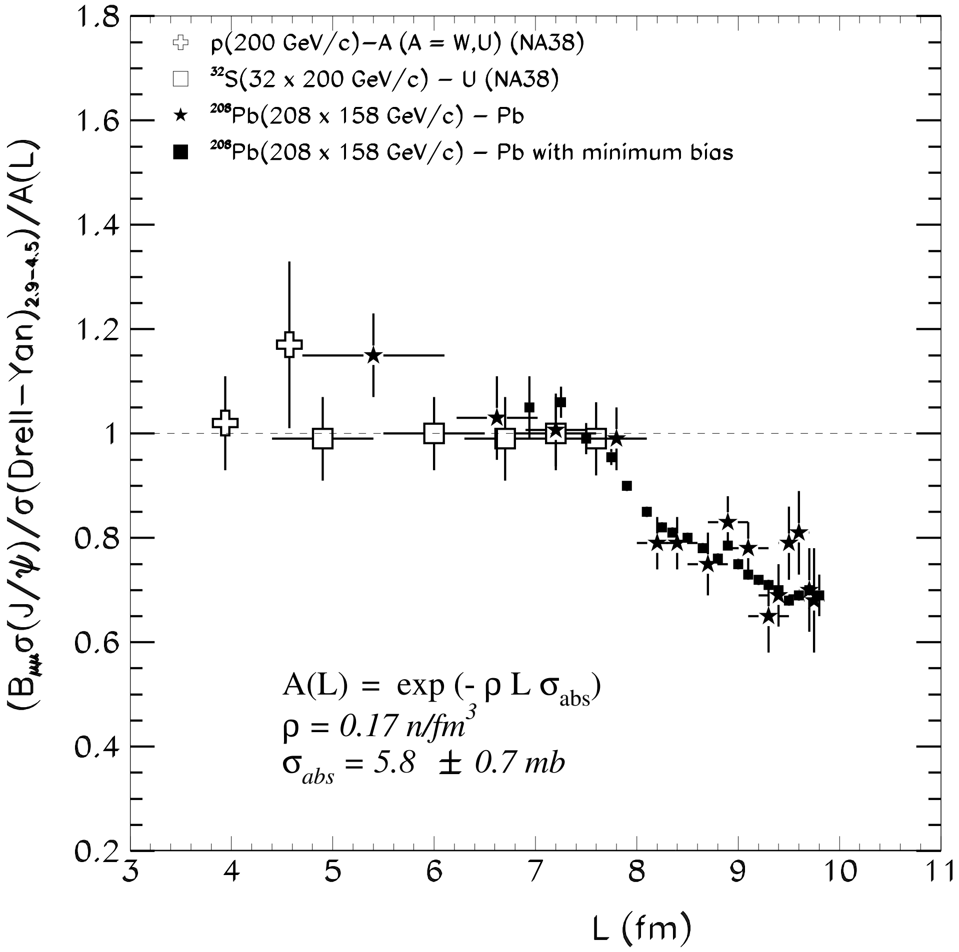

Figure 1.5: J/Ψ suppression in NA50 plotted against the estimated mean length of the J/Ψ path in the fireball. In the absence of new physics, J/Ψ occurrence should fall exponentially with L. The significant deviation at ∼ 8 fm could therefore be evidence of a change of phase in the system

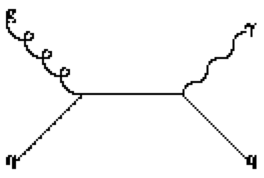

Figure 1.6: Direct photon production in a QGP

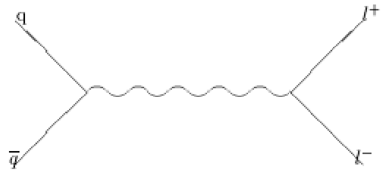

Figure 1.7: lepton pair production in QGP

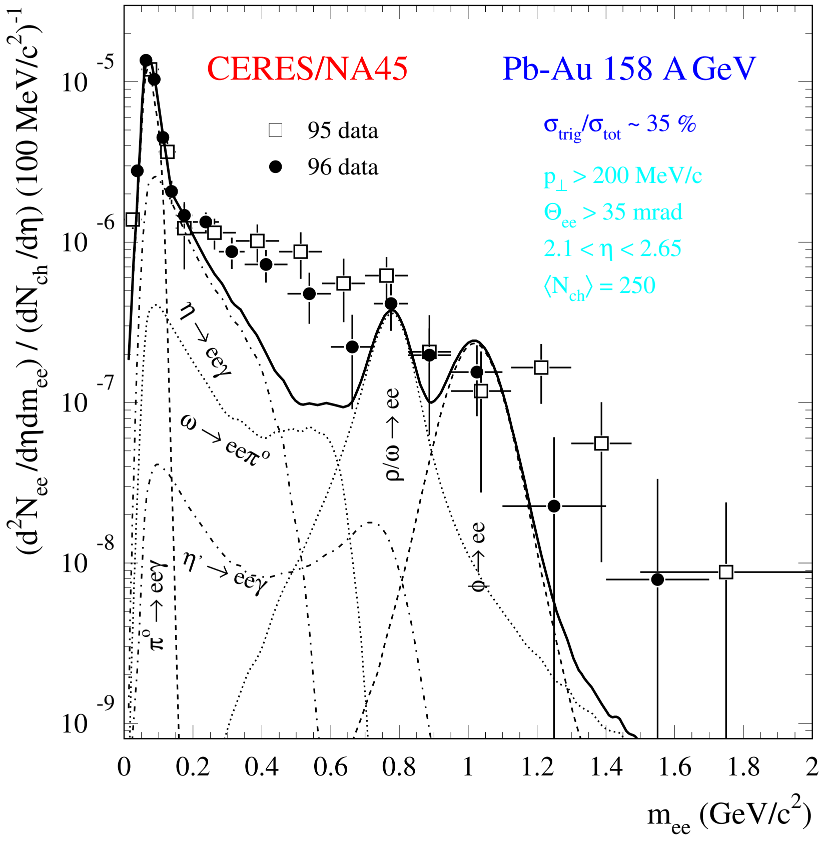

Figure 1.8: e^+e^- mass distribution observed by CERES against known background sources

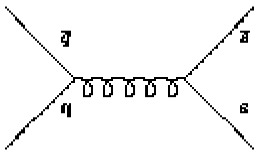

Figure 1.9: Strange particle production in QGP

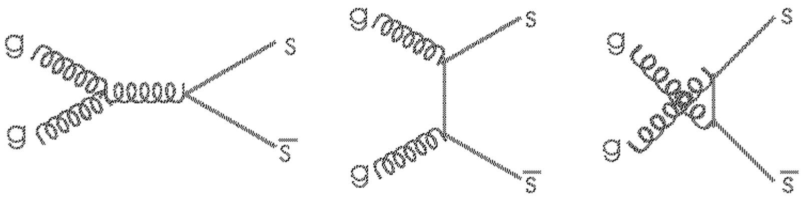

Figure 1.10: Strange particle production in a gluon-rich QGP

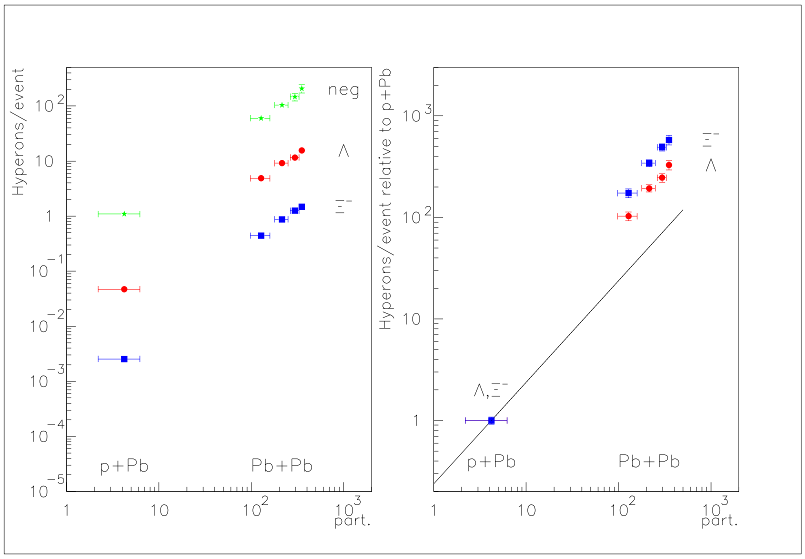

Figure 1.11: Hyperon yields of p-Pb and Pb-Pb collision normalised against the number of participants

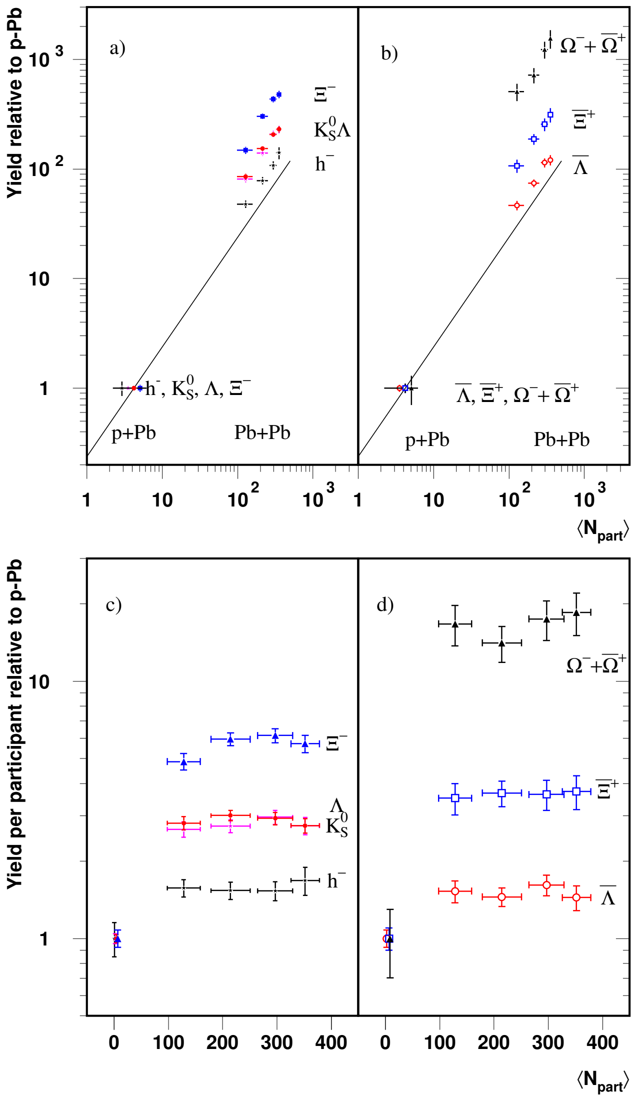

Figure 1.12: Strange particle Enhancement observed so far by the WA97 collaboration Top: Pb-Pb Yields normalised to p-Pb yields Bottom: Strangeness enhancement for different hyperons

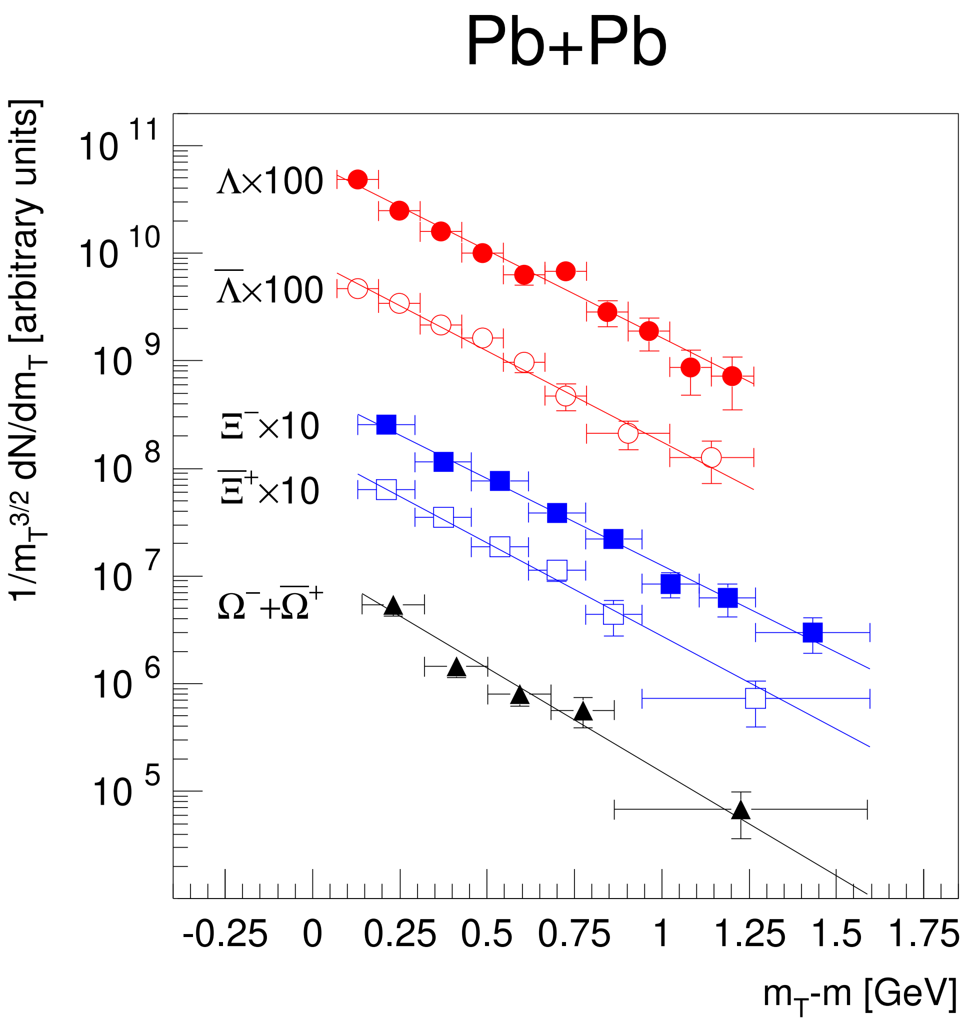

Figure 1.13: Inverse slopes (effective temperature) for the hyperons detected by the WA97 experiment. In this fit α has been assumed to be 3/2. The "correct" value of α should be 3/2 if the measurement covers the full range of rapidities, and 1 if only a small range of rapidities ($\sim dy$) is covered.

Chapter 2

The WA97 experiment

2.1 WA97 and NA57 approach

As outlined in the previous chapter, the method to test for QGP chosen by the WA97 and NA57 collaborations is strangeness enhancement. For this measurement, one needs to count the number of strange particles released in a heavy ion collision (where a QGP might have been formed) and compare this with the number of strange particles released in a control event, where QGP formation is not expected.

The leap forward in the experiments described in this chapter stems from their use of lead beams, enabling them to observe collisions between truly heavy nuclei forming significantly larger fireballs than before, such as lead-lead (414 nucleons in total). By comparison, earlier experiments such as WA94 [24] and WA85 [23] used S^{32} beams. Control events are provided by proton-beryllium and proton-lead reactions.

Unlike, for example, NA49, which was designed specifically with a large acceptance window [25] (and analyse most of the 1000+ tracks produced in a Pb-Pb collision) ,WA97 has been designed to only look for high transverse momentum (p_T) tracks produced in the region of central rapidity ($Y = \frac{1}{2} ln \frac{E+p_L}{E-p_L}$,where E is the energy and p_L the longitudinal component of momentum). As at mid-rapidity thermal, rather than kinematic processes dominate and the temperature is greatest, this is where QGP is most likely to have occurred (see Fig. 2.1). As p_T is correlated to temperature, a high p_T cut will enhance the proportion of detected tracks from the hottest region of the fireball.

Because of the relatively low number of tracks to analyse, identifying rarer particles such as Ξ s and Ω s becomes much more efficient. Since strangeness enhancement should increase with the baryon strangeness content, this feature is extremely important. (In fact, WA97 collected by far more statistics of Ξ and Ω events than any other heavy ion experiment in the world).

The limited range of possible Y-p_T values gives rise to the curved shaped acceptance windows seen in Fig. 2.2 The shape of the boundaries is determined by the relationship between p_T and Y, $p_T = \frac{m sinh(Y) sin(\theta)}{\sqrt{cos(\theta)^2 - sin(\theta)^2 sinh(Y)^2}}$ where m is the mass and θ is the angle of the telescope with respect to the beam. (The proof of this relationship is found in appendix 2).

The limited acceptance also means that, before any analysis can be performed, the number of undetected events with the same rapidity and transverse momentum of each given event will have to be found (a procedure known as "weighting"). The details of this procedure are given in chapter 5, where the negatives sample is weighted.

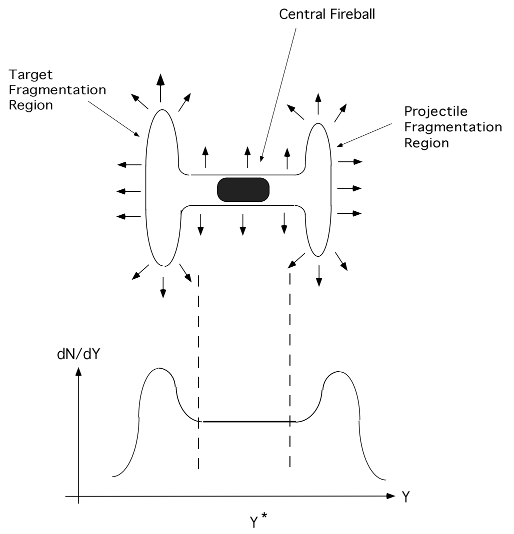

Figure 2.1: Dependence of particle multiplicity on lab frame rapidity

2.1.1 The p-Be control run

At the start of its operation, the WA97 experiment's only control run was p-Pb. However, a rigorous analysis needs to take into account the fact that, while a Pb-Pb system is symmetric with respect to the centre of mass, a p-Pb system is not. Therefore, there is no symmetry with respect to the central rapidity Y^* in the Pb-Pb rapidity distribution, and its peak does not correspond to the central fireball. Not taking this into account and choosing an incorrect mid-rapidity could lead to a spurious strangeness enhancement. It is therefore desirable to have a control run beam-target combination as symmetric with respect to the centre of mass as possible.

In addition, a rigorous analysis could not ignore a systematic shift in particle distribution resulting from the Cronin effect [27]: It was found that production of hadrons at large p_T was enhanced in proton-nucleus collisions, and the enhancement increased both with respect to the mass of the nucleus and the mass of the resulting particle (so proton production was more enhanced than meson production). As strange baryons are more massive than protons, it was felt

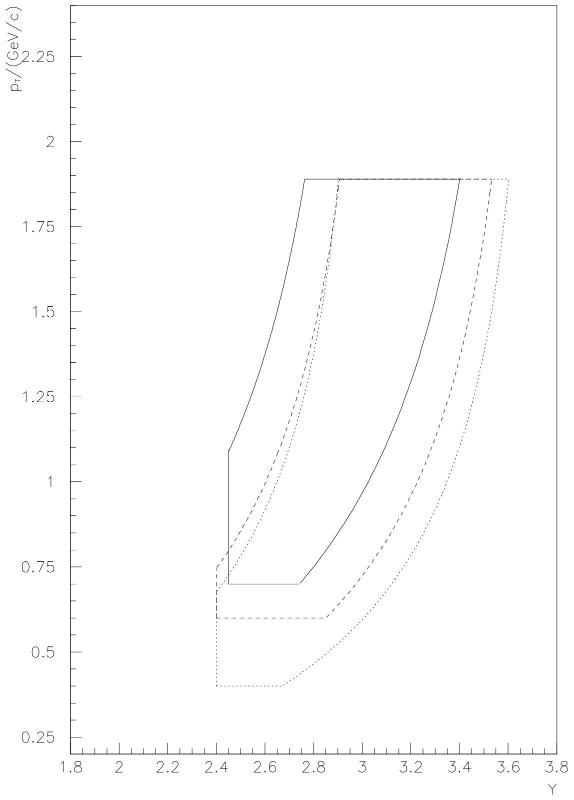

Figure 2.2: Acceptance windows for Λ (dotted), Ξ (dashed) and Ω (solid), [29]

that the Cronin effect contribution (as yet not modelled theoretically) could be significant.

For these reasons, it is very desirable that the control run target be as light a nucleus as possible. The Be nucleus, as the lightest the experimental layout would allow, was therefore used. As shown in the next section, this run made an addition to the apparatus of a beam telescope necessary.

2.2 Particle identification

Because of the theoretical considerations outlined in the previous chapter, the experiment concentrates on strange baryons Λ(uds), Ξ^-(dss) and Ω^-(sss) and their anti-baryons. Flavour-changing weak decays are used for detecting them, specifically

$\Lambda \to p\pi^-$

$\Xi \to \Lambda\pi^-$ or ΛK^-

$\Omega \to \Lambda K^-$

2.3 The WA97 experimental layout

The layout of the WA97 experiment is outlined in the Fig. 2.3 while a more detailed top-down view is shown in Fig. 2.4 The detectors in the WA97 experiment are used either for tracking or for triggering functions. The bulk of the tracking is done by the silicon telescope, with multi-wire proportional chambers (”pad chambers” in Fig. 2.3) placed downstream of the target. Triggering is done by the multiplicity detectors (scintillator petals and 2 dedicated microstrip planes), as well as the beam counters and telescope [28]. In addition, a beam telescope (not shown in the diagrams as it was added after the proposal) is used to reconstruct the beam for p-Be reactions.

The following sections describe each component of the experiment in detail.

2.3.1 Beam

The beams used are provided by the CERN Super Proton Synchrotron (SPS) which accelerates protons to a momentum of 450 GeV/c and Pb ions to 158 GeV/c per nucleon. The proton beam, at 160 GeV/c, was obtained by colliding the SPS beam with a secondary target. Because of this, the proton beam was heavily contaminated with pions. One of the main tasks of the p-Be trigger is to veto events produced by contamination.

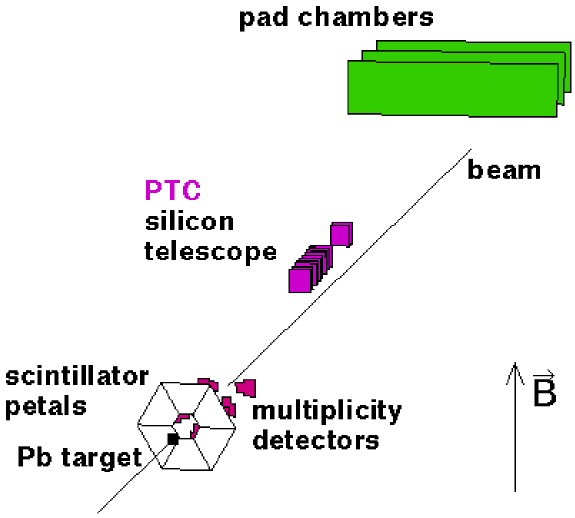

Figure 2.3: Layout of WA97 detector components

2.3.2 Spectrometer

The WA97 experiment used the OMEGA spectrometer, a superconducting magnet with two Helmholtz coils, which produced a 1.8 Tesla field. The target and detectors were placed inside the 36 m^2 region of field produced by the magnet. The experiment is symmetric with respect to the polarity of the field, so at first glance reversing it would not be necessary. However, to correct for residual small errors in the alignment of the components,the field is periodically reversed and data are taken in both polarities.

2.3.3 Reference coordinates

The system of coordinates used in all the analysis henceforward is based upon the spectrometer. The origin is at the centre of the magnet, the x axis is defined along the direction of the beam while z is the direction of the main component of the magnetic field. It is a left-handed coordinate system, so the y axis is

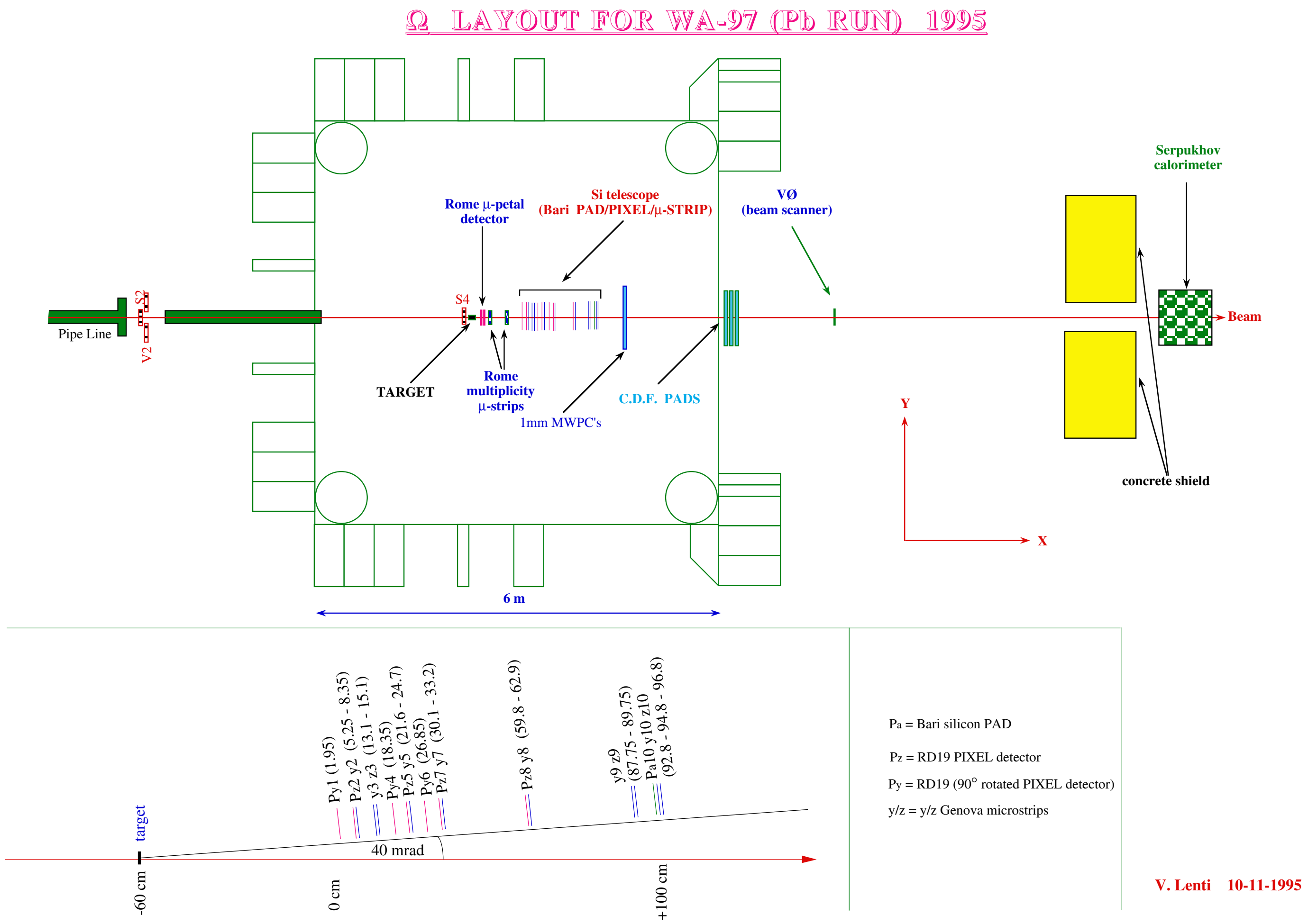

Figure 2.4: Top-down view of WA97. The target was actually put at -90 cm for the events analysed here

actually in the $x \times z$ direction. The beam crosses x=0 at y=0, z=-0.5 cm. The first telescope plane (pixel) is at x=0, while the first beam reconstruction microstrip is at x=-131.5 cm.

2.3.4 Target

In the coordinate system described in the last section, the target is at x=-90 cm. For lead, the thickness was chosen to be 1% of the interaction length of a

Pb ion (0.4 mm). For Berillium in the p-Be control reaction the thickness is 8% of the interaction length of a proton (3.6 cm).

2.3.5 Beam Counters

The lowest trigger level is based on the beam counters, and determines whether a beam is present. Consequently, they need to be the fastest component in the detector. There are 4 counters, 2 of which are upstream of the target (called S2 and S4). V2 is a veto counter, also upstream of the target, which detects particles not running along the beam axis (it has a hole in the middle to allow the beam to go through.) Finally, V0 is downstream of the target, and its task is to detect whether an interaction has taken place or not (if a beam particle interacted one would not expect it to pass through V0). While the requirements of these detectors are common to both the proton and the lead beams, the optimum type of detector varies: Quartz Cerenkov counters are consistently more precise than scintillators. However, as Cerenkov radiation intensity depends on particle momentum and length of the particle path inside the detector, the signal from such quartz counters is not powerful enough to detect a proton. Hence, V0 and S2 are Cerenkov counters for the Pb run and scintillators for the p run. V2 and S4 are scintillators for both runs, although of course the trigger threshold is different.

A different kind of Cerenkov counter, CErenkov Differential Counters with Acromatic Ring focus (CEDARs) was used in the proton beam to weed out pion contamination: CEDARS are based around long tubes filled with gas rather than quartz ,making them less fast than quartz detectors but sensitive enough for the proton beam. 8 photomultiplier tubes were placed around the beam at an appropriate angle, so that only Cerenkov radiation from a proton would reach the tubes.

2.3.6 Scintillator petals and multiplicity detectors

The multiplicity detector is used in the pb-pb triggering process, to select out central events. The event particle multiplicity is taken as measures of centrality. The hexagonal array of scintillators samples the number of particles that hit each of its 6 "petals". In a central event, one would expect the distribution of decay components to be roughly isotropic, so the number of hits on each petal coming from the interaction should be approximately equal.

In addition, for a more detailed off-line analysis of the centrality of each triggered event, 2 planes of silicon μ strips dedicated to multiplicity detection follow the petals. The pseudorapidity range covered is $2 \leq \eta \leq 4$ ($\eta = \frac{1}{2} ln \frac{|p|+p_L}{|p|-p_L} \simeq Y$ at WA97 energies)

2.3.7 Silicon Telescope

Tracking of triggered events is done by a silicon telescope, which employs pixel planes (which do the core of the tracking) complemented with microstrips planes. The telescope itself is placed above the beamline 90 cm from the target (compromise between number of tracks and reconstruction efficiency) and inclined, at an angle of 40 mrad with the beam detectors line.

Each silicon plane consists of 12 ladders, divided into 2 arrays. Each array is 5cm $\times$ 5cm, and there is an overlap between the ladders which compensates for the array's separation (several millimeters). Each ladder consists of 96 columns and 64 rows of rectangular diodes (the pixels), ion-implanted on a high-sensitivity n-type silicon substrate. There are 73,728 such pixels per plane, and the size of each pixel is 500×75 μ m. (A schematic top view of a pixel plane is provided in Fig. 2.5)

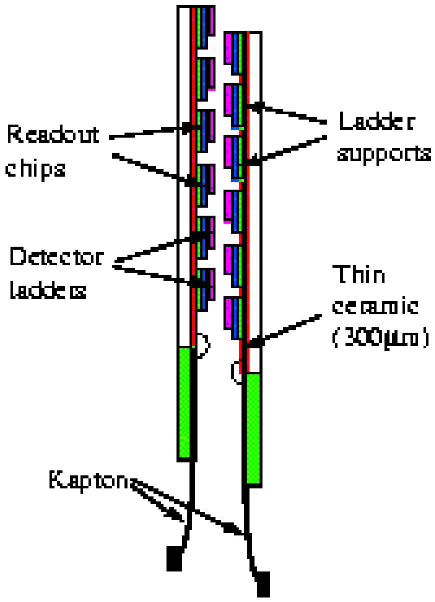

Figure 2.5: top-down view of pixel plane

The telescope provides planes of both the 2 possible orientations, to compensate for the fact that the pixels are rectangular in shape (and hence of lower resolution in one direction than in the other.

Each ladder also contains 6 chips, with 16 $\times$ 64 preamplifier cells (one per pixel). Each cell contains a front-end amplifier and a comparator with an adjustable threshold, adjustable delay line and some coincidence and memory elements. These are used to store the bit indicating that a particle hit has occurred during a time frame determined by an external strobe.

2.3.8 Beam reconstruction microstrips

This element was added into the detector after the start of WA97 and so was not included in the proposal. The inclusion of it was motivated by the p-Be control run: As explained in chapter 4, the thickness of the Be target makes the uncertainity of the primary vertex unacceptably large. Determining the primary vertex would be trivial in a collision of heavy ions, but in a p-be collision the track multiplicity is not high enough to permit finding the origin of the tracks without also knowing the exact beam trajectory through the target.

Hence, a beam telescope was added to the experiment to permit the beam to be reconstructed. The beam telescope was taken from the experiment WA102 [30] , and consists of 10 microstrip planes grouped into pairs. All pair modules are attached to a rigid optical bench, which serves as a coordinate reference for the microstrip planes.

2.4 Trigger logic

The trigger is based around three basic requirements: A beam has to be detected, an interaction has to occur and the interaction has to be "interesting" for the aims of the experiment. In the pb-pb case, the third requirement means the collision has to be central. In the p-Pb case, a minimum particle production is required.

It should be noted that triggering is also limited by the time it takes to read all detectors ($\sim$ 1 millisecond per event in p-pb), a time significantly longer than the average time between two "good" events.

2.4.1 Beam

There must be a signal from S2 and S4, to confirm that a beam was actually present in the event (the 2 detectors minimise noise-triggers). To ensure the beam is aligned, no signal from V2 must be present.

In addition, the CLEAN BEAM sub-level filters out multiple events within a time window of ± 30 ns (sensitivity period of the scintillators). These events are vetoed by passing the signal of the S2 counter to an updating discriminator. If a second signal arrives during the time δt after the first, the inverse of the signal from the updating discriminator will veto it.

2.4.2 Interactions

If the V0 counter is fired, it means the beam particle has passed through the target without interacting. Hence events where the V0 is fired are vetoed.

2.4.3 Further pb-pb requirements

The principle behind the multiplicity triggering has been described in the section on Scintillator petals. For the event to be accepted, at least 5 petals (out of 6) will have to show a multiplicity of at least 10 minimally ionising particles.

2.4.4 Further p-Be requirements

Since the WA97 experiment studies hyperon production, the trigger should select out such events in which at least one hyperon was produced. All hyperon decays described earlier have two decay products ,one of which (the baryon) takes the great majority of the hyperon's momentum. Hence, a suitable trigger requirement would be the presence of two decay particles, one of which (the baryon) is required to pass through the whole telescope (in other words, a signal from every telescope plane is expected). The presence of two particles is ascertained using the pulse higth of the scintillators placed downstream of the target. In addition, a signal from the CEDARS is used to make sure the event is not the result of pion contamination.

Events which pass the CEDAR part of the trigger but do not contain two particles or a particle going through the whole telescope still get recorded as "background" events. They will be used in the weighting chain, as described in chapter 5.

2.5 NA57

The WA97 collaboration observed a significant strangeness enhancement at midrapidity for central collisions at 158 GeV/nucleon. However, what happens "in between" the high-energy high-centrality window observed in WA97 and the regions which are certain to be non-QGP is still unknown. The purpose of the NA57 experiment [31] is to probe these regions. In particular, trigger multiplicity requirements are loosened to observe a greater centrality range. The use of the lower energy (40 GeV/nucleons) SPS beam also allows lower energy observations.

The layout and trigger logic of the NA57 experiment are nearly identical to the WA97 experiment. The main differences are:

- microstrip planes have been phased out, in favour of pixel planes
- The Omega spectrometer has been replaced by the GOLIATH magnet
- There are no Pad chambers.

The first run was conducted in November 1998, and 220×10^6 triggers were collected.

Chapter 3

Λ and Ξ reconstruction in p-Be collisions

3.1 Decay signatures

As outlined in the previous chapter, the WA97 experiment looks for flavour-changing decays:

$\Omega^- \to \Lambda K^-$

$\Xi^- \to \Lambda \pi^-$

$\Lambda \to p\pi^-$

The signature of the Λ decay is therefore that of a neutral particle (invisible to the detector) decaying into two charged particles. Events with this type of topology are called V^0. Some analysis is required to distinguish Λ and $\overline{\Lambda}$ candidates from all V^0-type events, as $K^0 \to \pi^-\pi^+$ is also a V^0-type event. Ξ

and Ω s, which decay too close to the target to be detected, appear as decays into a V^0 and a negatively-charged track (these decays are henceforward called cascades). The analysis in this chapter is necessary to filter out genuine Λ and Ξ events, from a background composed mainly of:

- K^0 (for Λ) s
- 2 independent charged tracks both produced in the target which get reconstructed as a V^0
- γ conversions and other interactions in the detector reconstructed as V^0 s and cascades

3.2 Tracking

The particle trajectories are reconstructed through "hits" in the telescope. Helices (circles in the x-y plane and linear in the z plane) are then fitted to each set of hits to reconstruct each particle's trajectory and calculate it's momentum. Once the momentum is known, each track is parametrized by the following 7 quantities:

- The x coordinate of the first plane hit (Set at 0 by the coordinate system explained in the previous chapter, and called henceforward reference plane)
- The y coordinate of the first plane hit
- The z coordinate of the first plane hit
- The angle of the particle's direction at the first plane hit in the x-y plane to the x axis (dip)

- The angle of the particle's direction at the first plane hit in the x-z plane to the x axis (Phi)

- The total momentum of the particle multiplied by it's charge

Given these 7 parameters, a track can be extrapolated to any point within the spectrometer (provided the magnetic field at all points is known) using a Runge-Kutta numerical algorithm [32]. (Exactly the same format and procedure is used to describe the trajectory of the beam. In case of the beam, the reference plane is at -131.5 cm).
Afterwards, a minimising routine (described in more detail in the next chapter) is used to find the closest approach point between pairs of oppositely charged tracks. V^0 candidates are selected by performing a loose cut on the distance of closest approach (see Fig. 3.1 for a schematic representation). Once V^0 candidate's trajectories are reconstructed, cascade candidates are found by extending the procedure described above for close approaches of Λ s and pions.

3.3 Cowboy and Sailor topologies

When a V^0 decays into two charged particles, two basic topologies are possible depending on the charged track's directions with respect to the magnetic field. They can either meet again before separating (Cowboy topology) or separate immediately (Sailor topology) (see Fig. 3.2).
Acceptance for cowboy-style events is much greater in WA97, since the two tracks stay reasonably close together for a longer time. Hence, the WA97 experiment only concentrates on cowboy-topology events.

The same reasoning applies to cascade events, with the proviso that the Λ trajectory is a straight line.

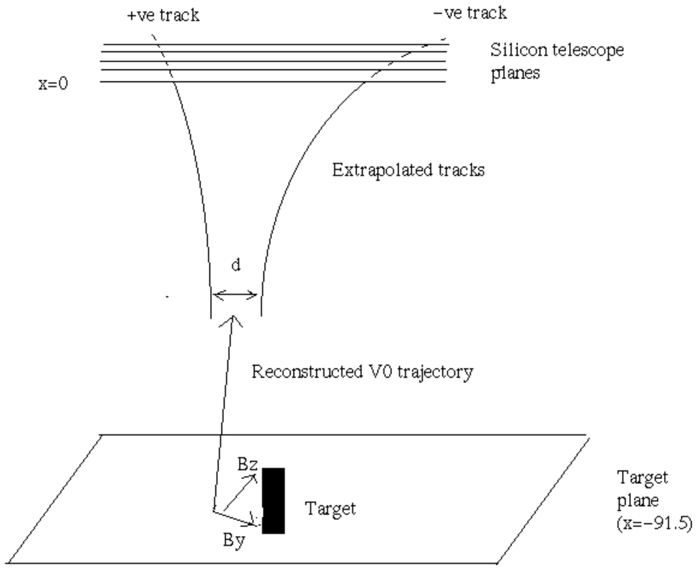

Figure 3.1: Schematic representation of how a V^0 decay is reconstructed in the WA97 detector. "d" refers to the distance of closest approach, while $B_{y,z}$ are the impact parameters

3.4 Target Λ selection

All events with a recognizable positive and negative track, and a Cowboy topology with a physical (ie downstream from the target) cowboy vertex were considered Λ candidates. WA97 P-Be runs managed to accumulate about 300,000 such events. The following cuts select physical Λ events from the background.

3.4.1 Closest approach point of the decay tracks

One of the main backgrounds to Λ events is constituted by independent pairs of particles reconstructed as V^0 s. Hence, a tighter cut on the closest approach distance increases the probability of each V^0 event in the sample to be a physical decay. A closest approach point distribution is shown in Fig. 3.3 and the cut is put at 0.06 cm.

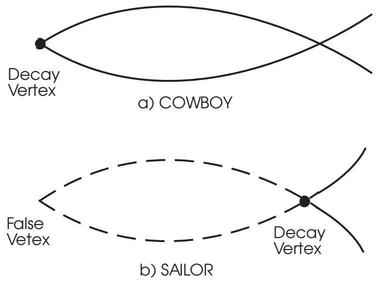

Figure 3.2: The Cowboy and Sailor topologies.

3.4.2 x-coordinate V^0 vertex

Fig. 3.4 shows that there are two peaks in the cowboy vertex distribution, one centered around -90. cm (where the target is) and the other approaching the 1st plane of detection in the telescope. Because of both the low probability of a decay and the low acceptance of the detector in that region, it is unlikely that many of the particles in the first peak correspond to physical decays rather than close independent tracks.

In addition, events with X_{cowboy} significantly before the high-acceptance peak will not be simulated reliably during the weighting procedure, and hence will have to be discarded anyway in the later analysis.

The second peak corresponds to a high acceptance region, but, especially approaching $X_{cowboy} = 0$, there is considerable contamination by γ conversions and other interactions within the telescope.

Cutting out the region outside $-30cm < X_{cowboy} < 0cm$ filters out the first peak. However, further cuts are needed to filter out γ conversions from the second peak.

The close parameter cut and the vertex cut, together, take away more than 90% of the candidate events, which are in fact pairs of independent particles. The remaining events are nearly all the result of some definite decay. More

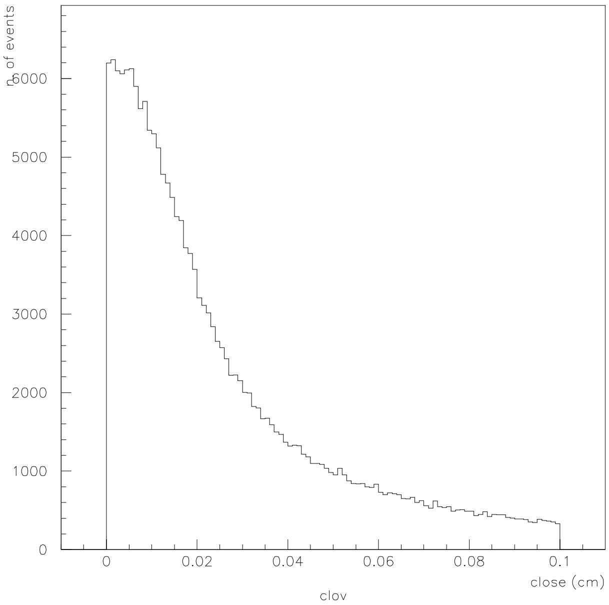

Figure 3.3: Closest approach distance between the decay tracks for V^0 candidates

than half of them, however, turn out to be something other than Λ s, and subsequent cuts are needed to eliminate them.

3.4.3 Armenteros-Podolanski cuts

The Armenteros-Podolanski plot [36] is a very useful method for distinguishing Λ candidates from K^0 events, γ conversions and independent particle pairs.
It is based on plotting, for each event, the transverse component of one of the decay product's momenta with respect to the V^0 direction (q_T) against $\alpha = \frac{q_L^+ - q_L^-}{q_L^+ + q_L^-}$, where $q_L^{\pm}$ are the components of momenta of the positive and negative tracks parallel to the V^0 direction.
It can be shown (appendix 1) that the V^0 s corresponding to different particles will separate into distinct elliptical loci, with the axes of the ellipse dependent on the masses of the original particle and the decay product.

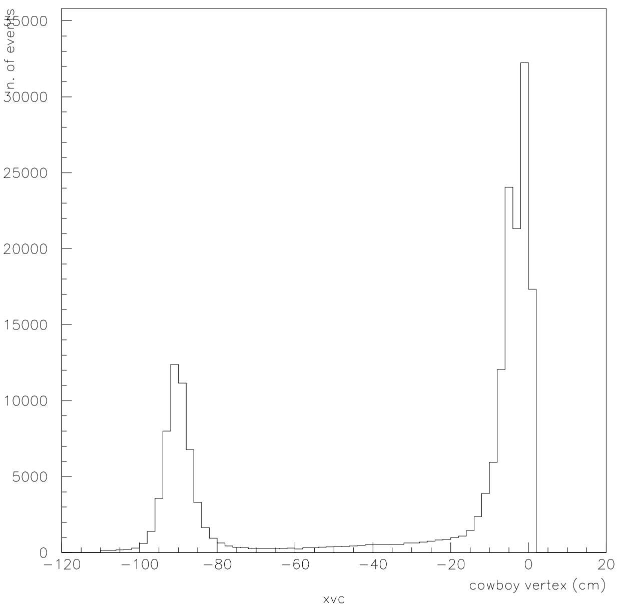

Figure 3.4: Cowboy vertex x-coordinate

As Fig. 3.5 shows, this makes cutting out signals not corresponding to definite particles and some K^0 events comparatively easy.
While Armenteros cuts are useful for cutting out such bogus events, it would be wrong to use extensive Armenteros cuts to select out Λ candidates, as a "tight" rectangular cut will have a similar effect of a mass cut (which would correspond to a cut around the ellipse).
Hence, a Λ selection based on tight Armenteros cuts will leave out Λ events with outlying masses, while retaining background events which happen to yield a "right" mass. The Armenteros cuts used for Λ s are $|\alpha| \geq 0.45$, $0.035 < q_T < 0.12$ GeV/c, with the appropriate α reversal of $\overline{\Lambda}$.

3.4.4 K^0 cut

Since some K^0 events overlap with Λ events on the Armenteros plot, an additional cut would be useful to remove this region. Removing events which yield

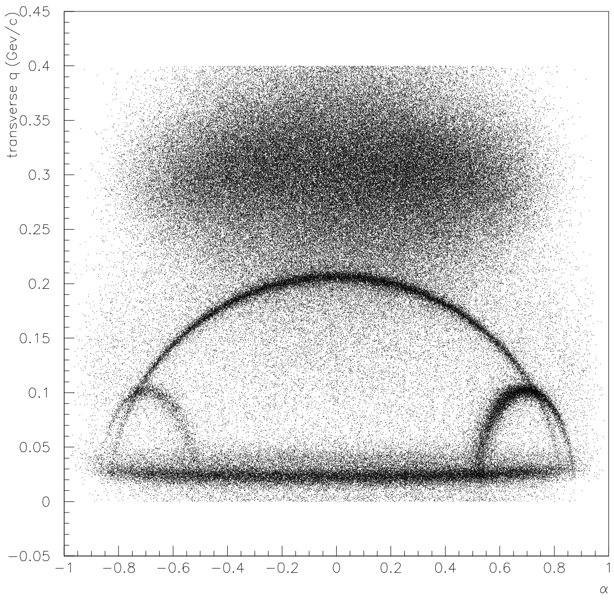

Figure 3.5: Armenteros-Podolanski plot. The two small ellipses at the sides correspond to particles with equal masses, but oppositely-charged decay products. In other words, $\Lambda \rightarrow p\pi^-$ and $\overline{\Lambda} \rightarrow \overline{p}\pi^+$ The large ellipse at the center is the K^0. Events above the K^0 ellipse do not correspond to particles with a definite mass, and therefore originate from independent tracks reconstructed as V^0 s. The flat set of events below the 2 ellipses seems to indicate particles with 0 mass, ie γ conversions

a "good" K^0 mass provides a way of doing this.
The formula which relates the V^0 mass (m_{V^0}) to the momenta, masses and energies of it's positive and negative decay products $(p_{+,-}, m_{+,-}, E_{+,-})$ is, by relativistic kinematics:

$$m_{V^0}^2 = (E_+ + E_-)^2 - (\underline{p_+} + \underline{p_-})^2$$

$$= ((\underline{p_+}^2 + m_+^2)^{\frac{1}{2}} + (\underline{p_-}^2 + m_-^2)^{\frac{1}{2}})^2 - (\underline{p_-} + \underline{p_+})^2$$

$= m_+^2 + m_-^2 - 2\underline{p_+}.\underline{p_-} + 2E_+E_-$ (4.1)

As the WA97 experiment does not provide the means to observe the energy or the mass of each particle, but only it's momentum, each V^0 decay can be reconstructed as a Λ, $\overline{\Lambda}$ or K^0 by assigning to $m_{+,-}$ the values of the appropriate decay products.
However, if the V^0 is identified incorrectly (for example, a proton track is identified as a π^+, so the Λ is assumed to be a K^0), the expression (4.1) will yield an abnormal mass for it.
Hence, in order to ascertain the Λ candidate is not a mis-identified K^0, it's mass calculated "as a K^0 has to be more than 30 Mev from the K^0 mass peak as recorded in the latest Review of particle physics (497.7 Mev) [33] .

The Armenteros cut and the K^0 mass cut have filtered out the main background decays to the Λ, which formed about 60% of the events which passed the close parameter and decay vertex cut. The final two cuts remove the residual contamination, and ensure the Λ comes from the primary vertex and not from a subsequent decay (In which case the event is a cascade candidate).

3.4.5 γ conversion cut

It was found that a few γ conversions within the detector can escape the cut on x_{cowboy}, since their vertex will be interpreted by the analysis program as a sailor vertex, and the extrapolated cowboy vertex will be located in the fiducial region. Such events will have:

- x_{sailor} equal or greater than 0.
- A low q_T

As Fig. 3.6 shows, there is indeed an over-abundance of such events, and cutting this region will eliminate the contamination. Therefore, events which have a sailor vertex between 0 and 6.6 cm with a q_T of less than 0.06 GeV were excluded.

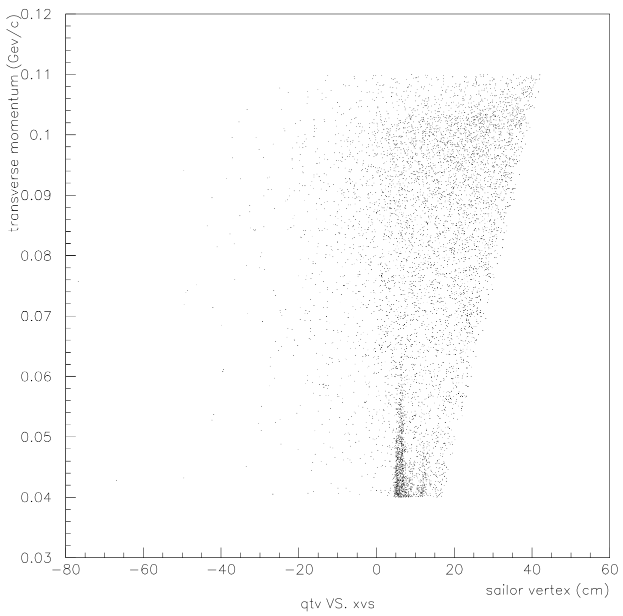

Figure 3.6: q_T of V^0 vs. x_{sailor}

3.4.6 Impact parameter cuts

Finally, assuming the Λ comes from the target and not from a cascade decay, a cut on the V^0 impact parameter provides a further guarantee of a reliable Λ. (here, the y and z components of the impact parameter are defined as the y and z coordinates of the track at the primary vertex x coordinate)

B_y and B_z are assumed to be $|B_y| \leq 0.15$ cm and $|B_z| \leq 0.10$ cm, corresponding to the size of the beam spot.

A distribution of the impact parameter after all the other cuts have been made is shown in Fig. 3.7. It is immediately apparent that the width of the y impact parameter distribution is considerably larger than the z. This is expected, since it is only the y component of the beam which is affected by magnetic field fluctuations.

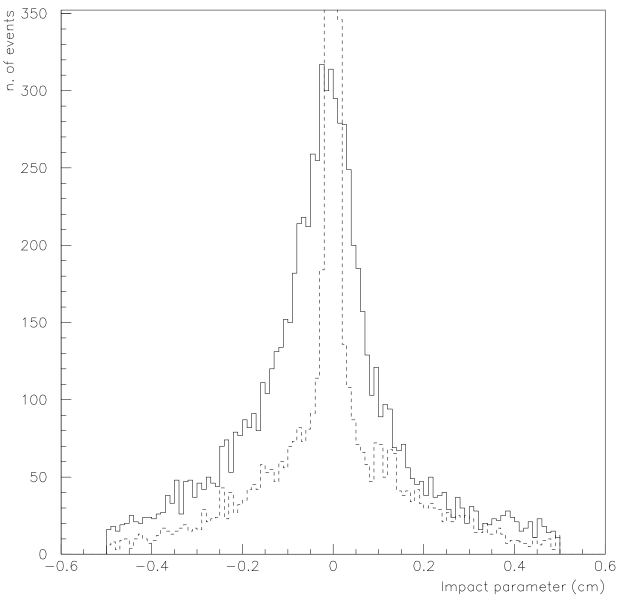

Figure 3.7: Solid line: B_y Dotted line: B_z

3.4.7 Results for Λ and $\overline{\Lambda}$

The mass distribution of Λ and $\overline{\Lambda}$ candidates is shown in figures 3.9 and 3.8. As can be seen, a clear mass peak distinguishable from the background signal is present.

3.5 Ξ selection

The trigger and the track-finding program has found about 30,000 cascade candidates, defined as V^0 candidates paired with non-primary charged tracks.

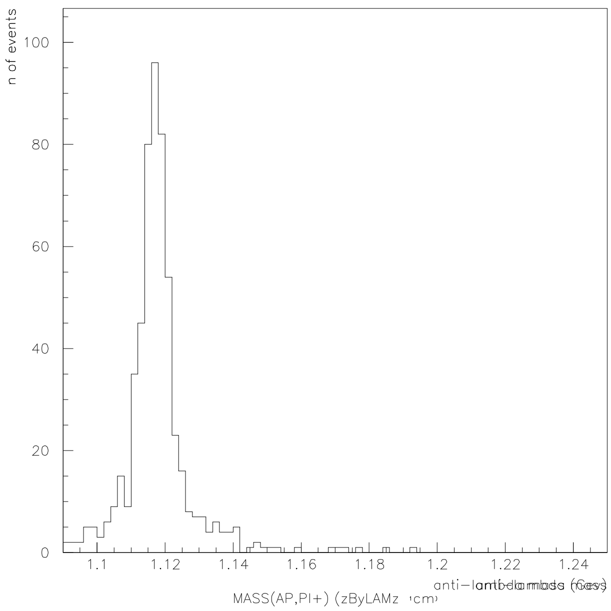

Figure 3.8: $\overline{\Lambda}$ mass distribution

The approach used to filter out good Ξ and Ω events from these is slightly different than the one used to obtain good Λ s out of the V^0 s sample.
In the V^0 case, geometrical cuts were performed to make sure the event corresponds to a physical decay. Afterwards, Λ decays were filtered out with the help of Armenteros and mass cuts.
In the cascade case, first it was ensured that the V^0 corresponds to a Λ. This is an efficient cutting method since non-Λ V^0 s have no chance of being part of a cascade decay.
Afterwards, geometrical and impact parameter cuts were performed to make sure the Λ and charged particle were not independent events.

3.5.1 Armenteros cut

The Ξ signal in the sample is not strong enough with respect to the background to do an Armenteros cut on the $\Xi \to \Lambda\pi$ decay. Also, the Ω sample

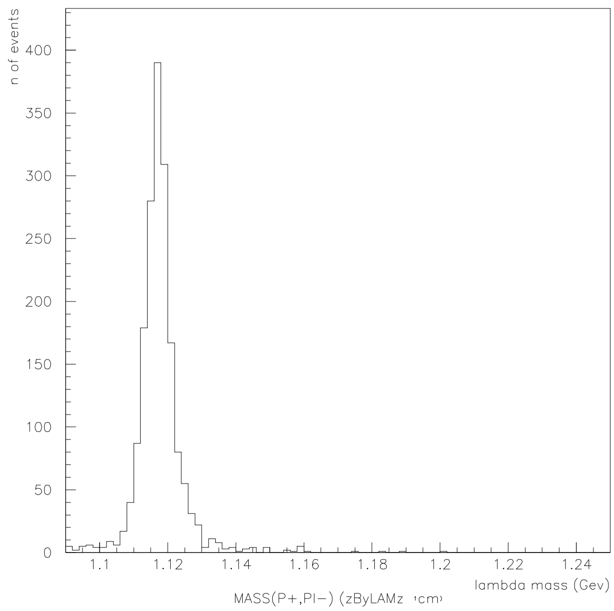

Figure 3.9: Λ mass distribution

is not nearly large enough to be distinguished from the Ξ s by an Armenteros plot, even after cuts. Hence, no cascade Armenteros cuts were performed.
However, an Armenteros cut is used to select good decay Λ s. This time, a "tighter" Armenteros cut on the V^0 is justified, as it was ascertained in the previous analysis that a strong V^0 signal does indeed exist.
It is therefore required that $0.04 < q_T < 0.11$, $-0.86 < \alpha < -0.54$ GeV/c for $\overline{\Lambda}$ and $0.54 < \alpha < 0.86$ GeV/c for Λ

This cut eliminates well over 90% of all cascade candidates. Sorting out genuine Ξ s and Ω s from independent (Λ, charged track) combinations, however, is considerably harder since the Λ gets practically all of the decayed momentum of the Ξ. An independent $\Lambda\pi$ pair, therefore, can look like a perfectly sensible Ξ.
To be sure to have eliminated such events, it is necessary to look at the closest approach, cascade decay vertex and impact parameter of both the cascade

decay and the subsequent V^0. A gold-plates hyperon decay must pass all 3 of such cuts.

3.5.2 Closest approach cut

The following cuts were made on the closest approach points between tracks:

- The V^0 in the cascade decay has to satisfy the V^0 closest approach cut given in 3.4.1.
- The closest approach between the cascade π and the reconstructed Λ must be less than 0.2 cm.

The distribution of the closest approach for the V^0 which might have come from a cascade decay is shown in Fig. 3.10, while 3.11 shows the $\Lambda\pi$ closest approach.

3.5.3 x-coordinate cowboy vertex of the cascade

The same arguments of the V^0 case apply here, with the proviso that the average Ξ decays before the Λ [33], so the minimum x-coordinate cut has to be lowered to -60 cm. In addition, the same cut as the one used for Λ selection was applied on the V^0.

3.5.4 Impact parameter cuts

A Ξ detectable by WA97 will decay into a Λ and a π. Hence, an appropriate impact parameter cut will demand a maximum impact parameter on the cascade (to make sure it corresponds to a Ξ coming from the target), but also

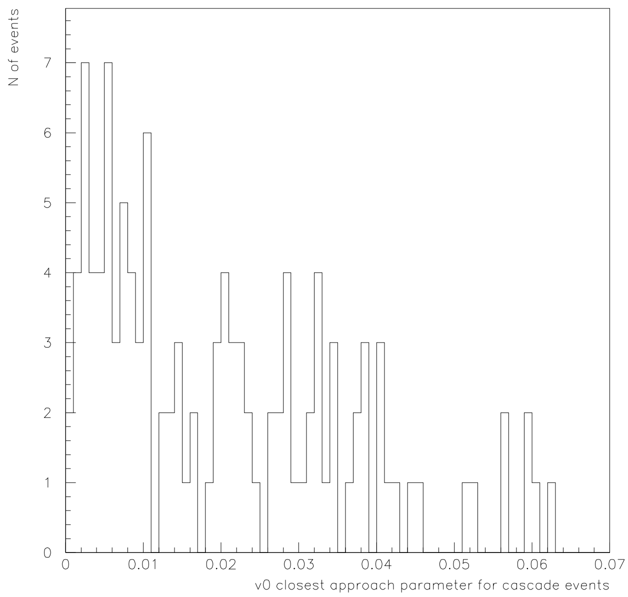

Figure 3.10: Closest approach distance between the decay tracks for V^0 s coming from cascade decays

a *minimum* impact parameter on the V^0, (to make sure it is not a Λ coming from the target and intersecting an independent π track)
In practice, however, the V^0 will carry nearly all of the cascade's momentum and its direction will be nearly the same as the cascade's so a minimum requirement on its impact parameter would be very unreliable. It is much better, therefore, to demand a minimum impact parameter for the π.
The cuts used are:

$|B_y| < 0.5$ cm, $|B_z| < 1$ cm for the cascade

$|B_y| > 0.5, |B_z| > 0.5$ for the π

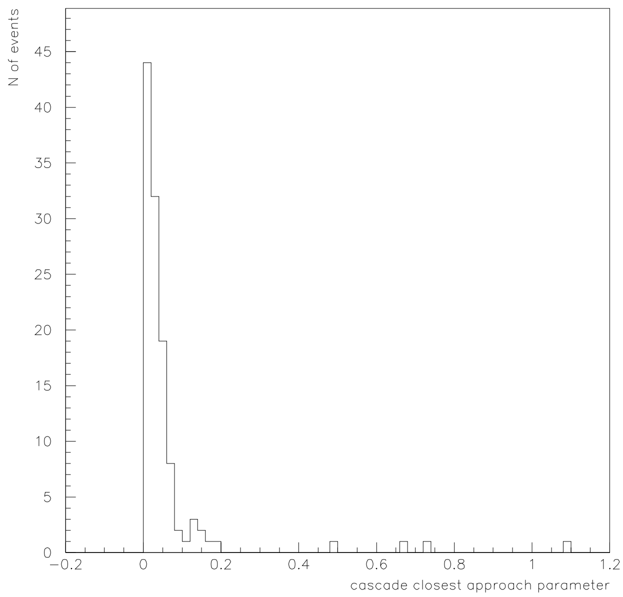

Figure 3.11: $\Lambda\pi$ closest approach

3.6 Results

As can be seen comparing the Armenteros-Podolanski plots in Fig. 3.12 (where no cuts were performed) and Fig. 3.13 (with the cuts above), a definite Ξ signal was found. The fact that no Armenteros cuts were done on the cascade decay itself, yet the ellipses ,not apparent before, are extremely clear, is a good confirmation of the signal's reliability. The mass distribution of the 152 cascade candidates is shown in Fig. 3.14 The great majority of those are Ξ events, but it is worthwile to try to separate the good Ω candidates as well.

3.6.1 Separation of Ω and Ξ signals

As mentioned before, WA97 has no way of measuring the mass of the decay product tracks and so cannot distinguish Ξ and Ω by their decay products. The sample of Ω s is also too small for an Armenteros-Podolanski, or other

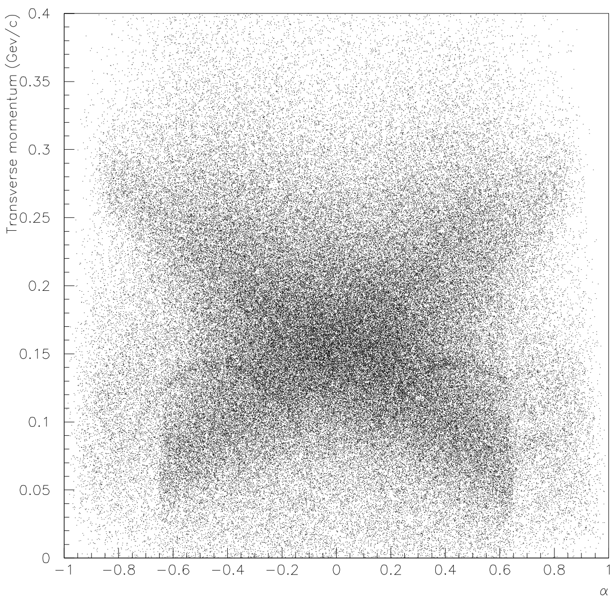

Figure 3.12: Ξ^+ Armenteros plot before cascade cuts. The ellipses apparent in the plot come from independent $\Lambda\pi$ pairs which dominate over genuine Ξ s. Since typically Λ momentum is so much larger than π momentum, such events can give rise to reasonable ellipses

topology analysis. Therefore, the only way to distinguish Ω and Ξ candidates is to compare the two possible estimates of the mass of each candidate (calculated assuming their product decays to be, respectively Λ π and Λ K) with the Ξ and Ω PDG masses [33]. For the event to be classified as an Ω, therefore, it is required that:

- $m_{\Lambda\pi} - m_{\Xi PDG} > 20 Mev$
- $m_{\Lambda\pi} - m_{\Xi PDG} > m_{\Lambda K} - m_{\Omega PDG}$

A plot of $m_{\Lambda\pi}$ against $m_{\Lambda K}$ is shown in Fig. 3.15. Figures 3.16 and 3.17 show, respectively, the Ξ and Ω distributions.

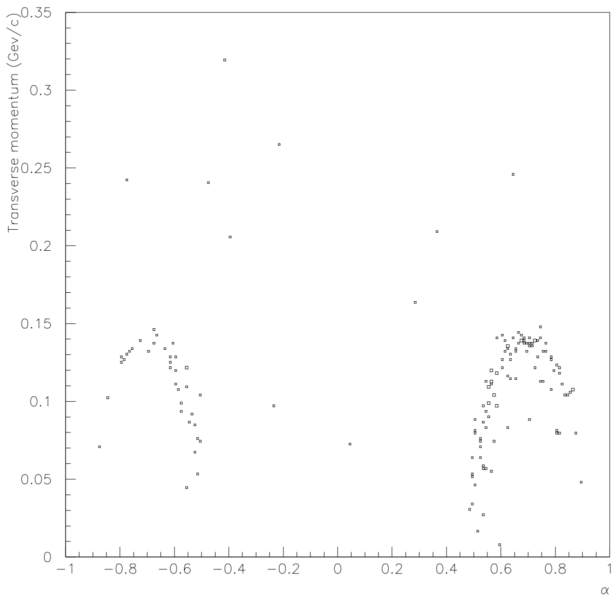

Figure 3.13: Ξ^+ (left ellipse) and Ξ^- (right ellipse) Armenteros plot after cascade cuts.

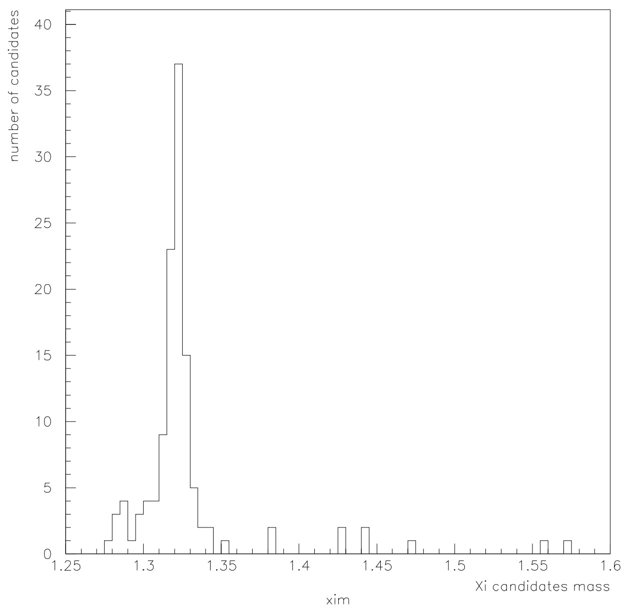

Figure 3.14: cascade mass distribution (Ξ and Ω)

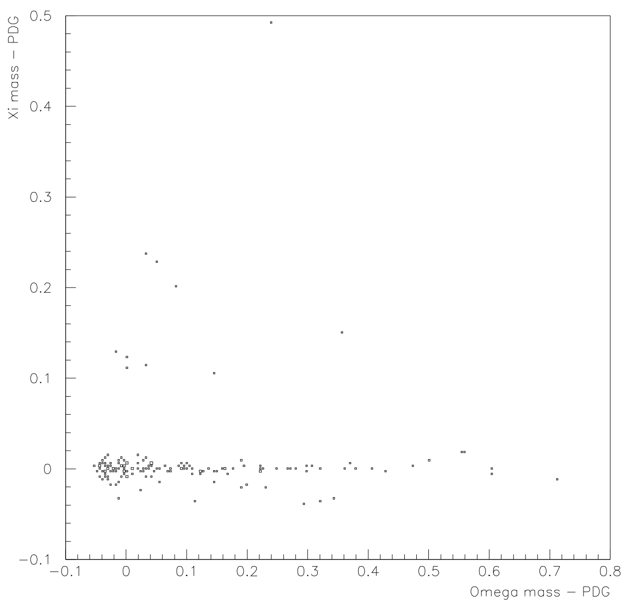

Figure 3.15: Differences between the masses of the cascade events calculated assuming $\Lambda\pi$, ΛK with the currently accepted values of m_{Ξ}, m_{Omega}

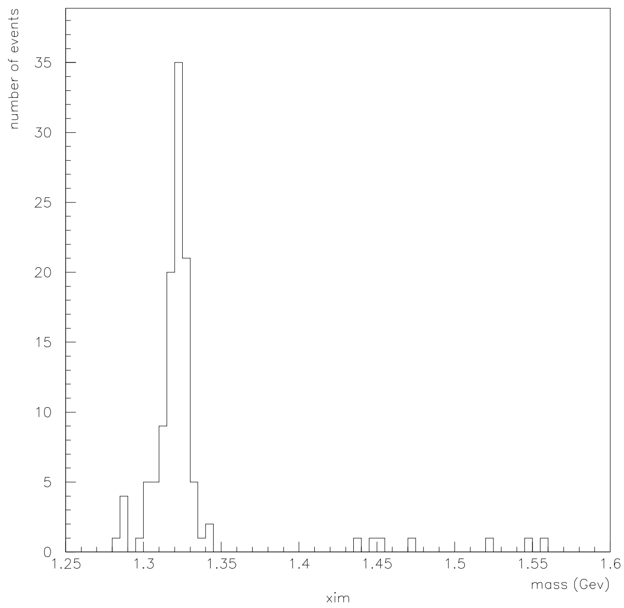

Figure 3.16: Ξ mass distribution

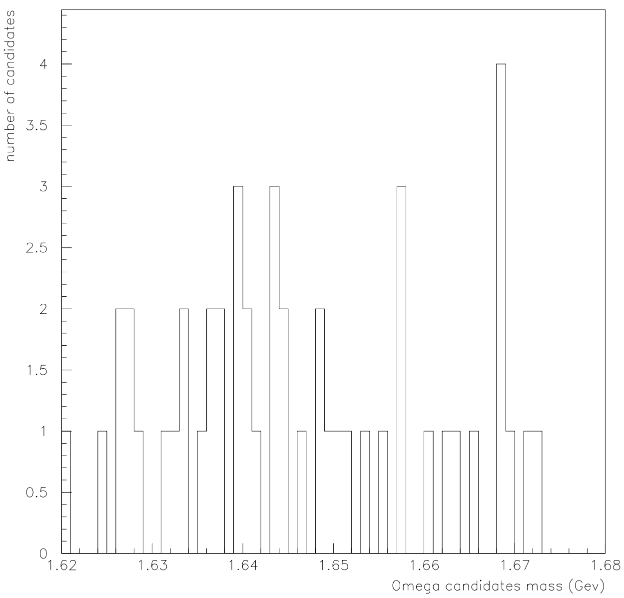

Figure 3.17: Ω mass distribution

Chapter 4

Computation of the Primary vertex in p-Be collisions

4.1 The primary vertex

As mentioned in chapter 2, the beryllium target is 3.6 cm thick, considerably more than the thickness of the lead target used for Pb-Pb interactions (400 μm).

As a result, the x-coordinate of the primary vertex is a lot less precisely determined in the control p-Be events than in Pb-Pb. (The y and z coordinates are determined by the size of the beamspot, and hence are identical for p-Be and for Pb-Pb). It is necessary to improve this precision, as the position of the primary vertex is needed when calculating geometric acceptances of the detector.

In this chapter, an analytical and a numerical procedure are used independently to calculate the primary vertex from the tracks for the beam and the Λ. An independent primary vertex calculation for negatively charged particles (assumed to be pions) in background events is also performed.

4.2 Numerical procedure

4.2.1 Functions to be minimised

The primary vertex is assumed to be at the midpoint of the closest approach vector between the trajectories of the beam and of the detected particle.
The beam trajectory is assumed to be a helix, i.e. a circle in the x-y plane (perpendicular to the B-field), and a straight line in the Z (parallel to the B-field) plane.
The Λ, as a neutral particle, has a linear trajectory in all directions, while the negative particle will follow a helical shape similar to that of the beam. The beam and the particle are parametrised in terms of two independent variables t_1 and t_2. Therefore:

$$x^{beam} = x^{beam} + R^{beam} cos(\theta^{beam} + \omega^{beam} t_1)$$

$$y^{beam} = y^{beam} + R^{beam} sin(\theta^{beam} + \omega^{beam} t_1)$$

$$z^{beam} = z_0^{beam} + v_z^{beam} t_1$$

In the Λ primary vertex calculation the particle trajectory will be:

$$x^{\Lambda} = x^{\Lambda} + (\frac{p_x^{\Lambda}}{|p|}) t_2$$

$$y^{\Lambda} = y^{\Lambda} + (\frac{p_y^{\Lambda}}{|p|}) t_2$$

$$z^{\Lambda} = z^{\Lambda} + (\frac{p_z^{\Lambda}}{|p|}) t_2$$

In the primary vertex calculation for the Negative, the particle trajectory will be:

$x^\pi = x^\pi + R^\pi cos(\theta^\pi + \omega^\pi t_2)$

$y^\pi = y^\pi + R^\pi sin(\theta^\pi + \omega^\pi t_2)$

$z^\pi = z^\pi + v_z^\pi t_2$

(It should be kept in mind that $t_{1,2}$ are simply parameters in functions to be minimised, without any physical significance).

The assumption that the beam and the π follow helical paths is valid in a region where the field is approximately uniform. Hence, the helice's parameters are fitted after using the Runge-Kutta procedure described in section 3.2 to follow the tracks to a region at the midpoint of the target (close enough to the primary vertex to discount field variations).

4.2.2 Minimising algorithm

After the trajectories are fitted, standard Gauss-Newton iterative algorithm [34] is used to minimise the distance between 2 points on the track, $F(x, y, z) = (x_{beam} - x_{particle})^2 + (y_{beam} - y_{particle})^2 + (z_{beam} - z_{particle})^2$, with respect to t_1 and t_2.

It constructs a sequence t^k of parameters, satisfying $t^{k+1} = t^k + \alpha^k p^k$, where α^k is the step length and p^k the search direction. The search direction is computed using the gradient vector of F $(\frac{\partial F}{\partial t_1}, \frac{\partial F}{\partial t_2})$, $\frac{\partial F}{\partial t_i} = \frac{\partial F}{\partial x_i}\frac{\partial x_i}{\partial t_i} + \frac{\partial F}{\partial y_i}\frac{\partial y_i}{\partial t_i} + \frac{\partial F}{\partial z_i}\frac{\partial z_i}{\partial t_i}$ (second derivatives are not used as they would make the program less robust).

α^k is calculated by fitting a cubic polynomial to F's projection onto the search direction. The above procedure is performed iteratively, and a convergence test is performed to determine whether the current step is an adequate approximation. The analysing program tries out the minimising routine 3 times,

at different starting $t_{1,2}$;
If more than one minimum is produced, the smallest is assumed to be the correct one.

4.3 Analytical calculation

It is also possible to calculate the primary vertex by a straight-forward algebraic calculation, by using the fact that the trajectory of a charged particle in a magnetic field is a circle in the plane perpendicular to the field, but a straight line in any of the planes parallel to it.

4.3.1 Λ primary vertex

The Λ will be a linear in all planes, while the beam will be circular in the x-y plane and linear in the y-z and x-z planes. Hence, it is possible to obtain x-z or y-z from the intersection of two lines, or x-y from the intersection between a line and a circle. In choosing which procedure to use, it must be kept in mind that R^{beam} and x_0^{beam} are $\sim$ 300 m, while all the other parameters are $\sim$ 1 m. Hence, the uncertainities of R^{beam} and x_0^{beam} are likely to dominate, and the way to keep the measurement more precise is to keep these low. As Fig. 4.1 shows, because of the low transverse momentum (w.r.t the total momentum) of the typical track, the x coordinate is the most sensitive to changes in the radius or the center of the beam track. It therefore makes sense to calculate it it in the x-z plane:

$$z^{beam} = \frac{p_z^{beam}}{p_x^{beam}} x^{beam} + x_0^{beam}$$

$$z^{\Lambda} = \frac{p_z^{\Lambda}}{p_x^{\Lambda}} x^{\Lambda} + x_0^{\Lambda}$$

The intersection point of these two lines should yield a good approximation for the x and z coordinates of the primary vertex. (it is noted that, as explained before, that all this holds true in regions of approximately uniform field. A Runge-Kutta procedure therefore still needs to be performed to find the position of the particle at a point close to the primary vertex, and the momentum needs to be calculated at that point).
The y coordinate can be found by solving the y-z linear equations in the same way as the x-z were done, or by feeding the x value found previously in the x-y circular equation $x_{beam}^2 + y_{beam}^2 = R_{beam}^2$.

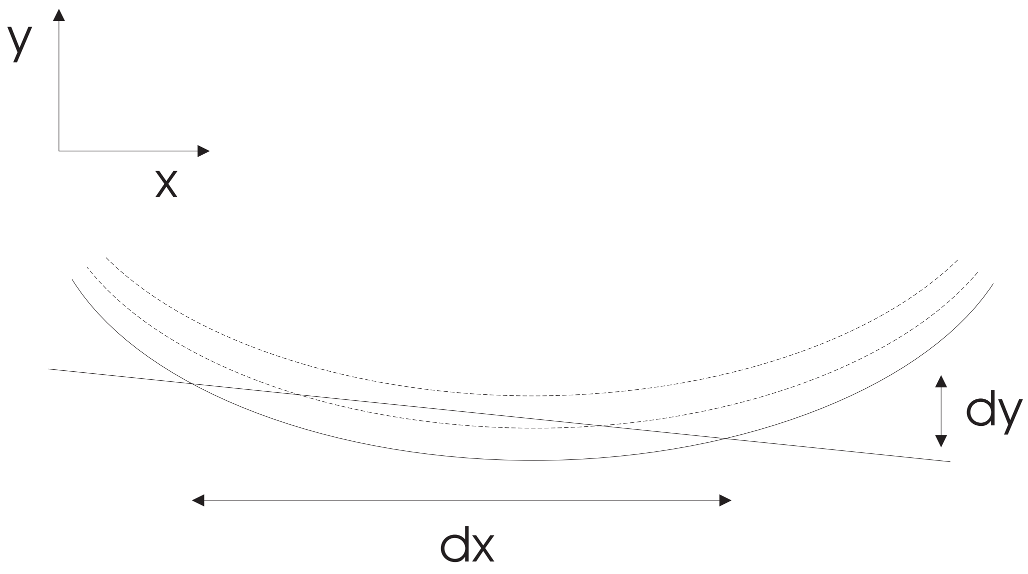

Figure 4.1: How inaccuracy in the radius of the circle can lead to significantly different values of x.

4.3.2 Primary vertex of negative particles

In this case it is two helices rather than a helix and a line which intercept. However, the procedure described in the previous section still applies as in the

x-z plane both the beam and the negative's trajectories are linear.
The x coordinate found in the x-z plane can then be fed into either one of the two circles in the x-y plane to find the corresponding y value (again, using the negative's trajectory in this calculation will be less sensitive to the uncertainty of the beam radius and center).

4.4 Results for Λ s

The efficiency of the numerical routine (defined as $\frac{N_{Success}}{N_{Total}}$ where $N_{Success}$ is the number of tries where an estimate of the primary vertex was achieved and N_{Total} is the total number of tries), is 98 %, with little dependence on which batches of events are used.
This is approximately equal to the percentage of events which gave a physical result in the numerical calculation. The computed coordinates of the primary vertex are shown in Fig. 4.2, 4.3, 4.4.
As figure 4.6 shows, for good Λ s the analytical and numerical calculations yield similar results.

(It should be noted that the beam crosses the Omega spectrometer at z=-0.5 cm). Fig. 4.5 shows the square of the closest approach distance.
As mentioned in the previous section, there are several ways to get the final y coordinate. For example, it is possible to put the x found by solving the system in the x-z plane into the x-y plane. Or it's possible to solve in the y-z plane independently from the x-z plane.
The uncertainty for each y calculation depends on the uncertainities of different coordinate measurements. Comparing two such calculations is useful as a check against any systematic errors in the measurements and procedures. Fig. 4.8 shows the difference between the y value obtained by solving the y-z plane independently and the y value obtained from solving in the x-y plane. The

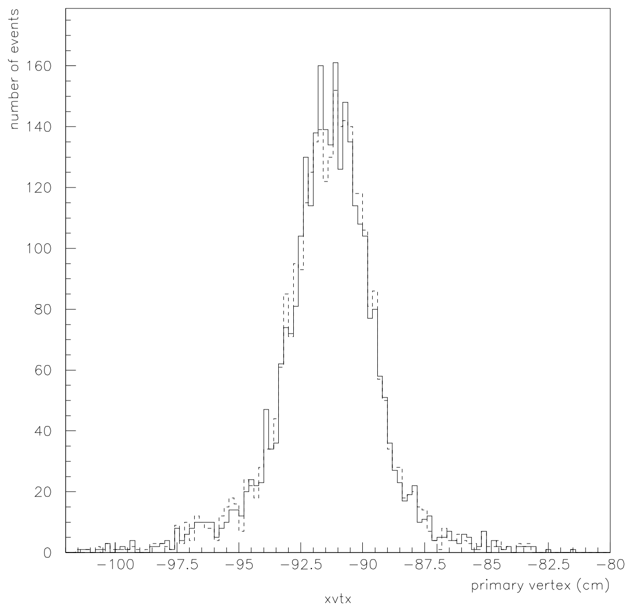

Figure 4.2: Analytical (solid line) and numerical (dotted line) x coordinate of the primary vertex

distribution is centered around 0, a sign that the calculation contained no systematic errors.

As the target position is assumed to be -91.6 $\pm$ 5 cm, there appear to be several "rogue" V^0 s whose primary vertex is not within the target. Fig. 4.7 shows that events with an outlaying x primary vertex tend to have a similarly outlaying y primary vertex, while such dependence is less apparent in case of the z primary vertex. (As particles bend in the x-y plane, this is to be expected). The unphysical events probably could originate from independent tracks mis-reconstructed as V^0 which filtered through the cuts. The primary vertex can therefore also be used as an additional cut.

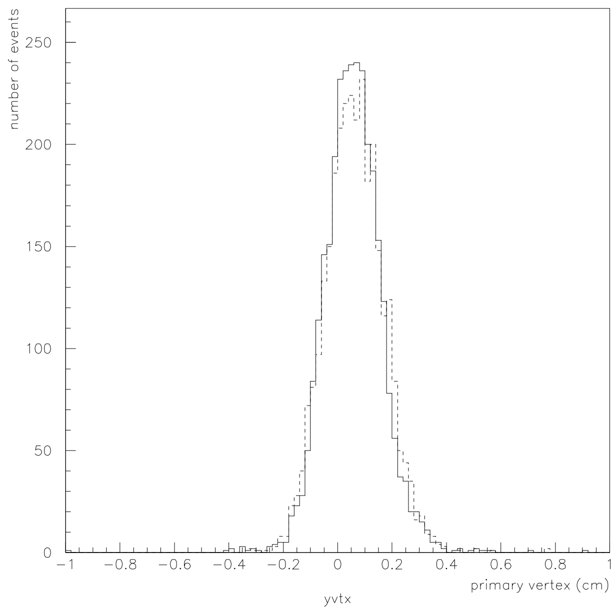

Figure 4.3: Analytical (solid line) and numerical (dotted line) y coordinate of the primary vertex

4.5 Results for negatives

The Coordinates for the x, y and z coordinates are shown in Figs 4.9 4.10 4.11, while Fig. 4.12 shows a comparison between the analytical and numerical results. As can be seen, the result is considerably less centered around the physical position of the target than in the Λ case. This is because many negatives come from Λ decays and secondary interactions within the detector. Cutting out these Λ s is fundamental for the analysis described in the next chapter, and ensuring the primary vertex is physical will be one of the ways to do this.

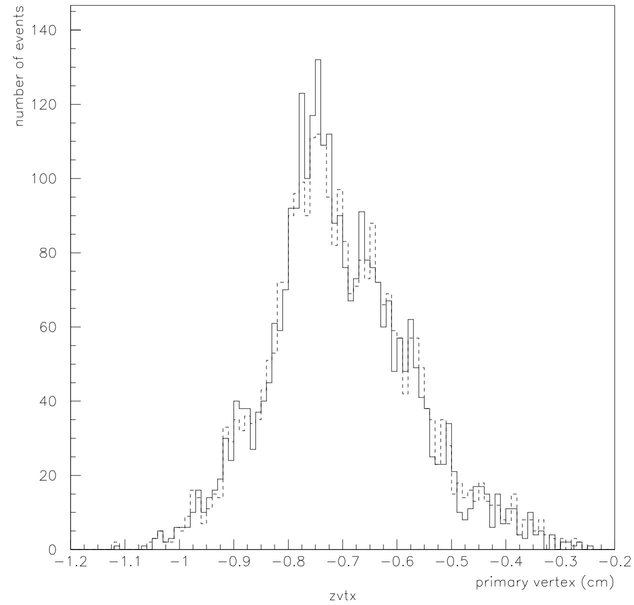

Figure 4.4: Analytical (solid line) and numerical (dotted line) z coordinate of the primary vertex

4.6 Correction for beam telescope mis-alignment

The parameters of the beam track reconstructed using the beam telescope are measured in the coordinate system used for the main telescope (described in chapter 2).

However, as the beam telescope and the main telescope are independent, small mis-alignments between them would result in reconstruction errors.

Because of the low P_T of the reconstructed tracks, a mis-alignment of a few millimeters in the y and z coordinates could result in an error of the order of a centimeter in the x coordinate of the primary vertex. Hence, a measurement and correction of eventual mis-alignments was required.

One way to measure the mis-alignment is to use a sample of events with 2 independent tracks coming from the primary interaction. In such events, the primary vertex can be estimated without the need of the beam telescope, simply

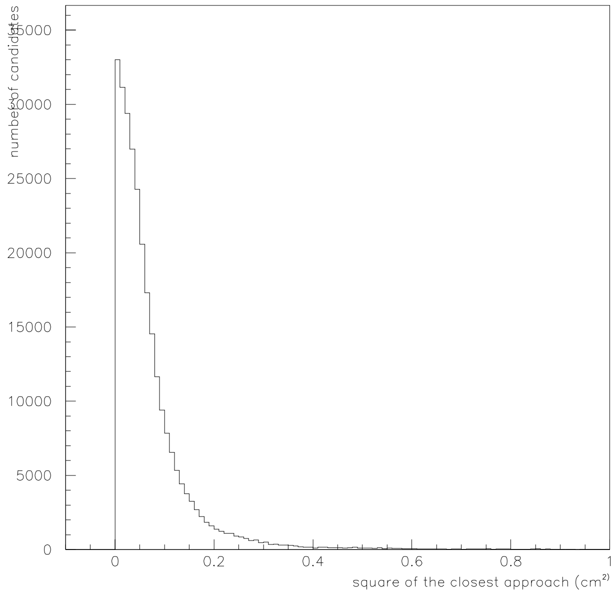

Figure 4.5: Square of the closest approach distance

by finding the closest approach point of the two tracks.

After the x coordinate of the primary vertex is found using this method, the beam trajectory is traced to it, and the resulting y_{beam}, z_{beam} are compared with the y and z coordinates of the primary vertex computed using the two independent tracks (y_0, z_0).

If the beam reconstruction microstrips and the telescope are perfectly aligned according to the same coordinate system, the distributions $y_0 - y_{beam}$, $z_0 - z_{beam}$ should be centered around 0. Any shift away from 0 would indicate a misalignment.

This procedure was performed on oppositely charged track pairs which did not satisfy the closest approach cut (discussed in the previous chapter) and had an intersection point within the target. They were therefore assumed to be independent tracks coming from the primary interaction, not associated with a V^0.

As fig 4.13 shows, a clear shift is indeed present. After a sample of events in

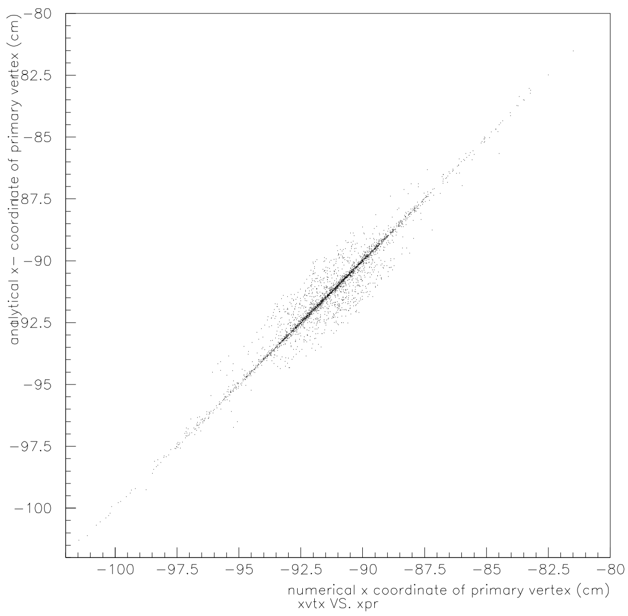

Figure 4.6: Analytical vs numerical calculation of x coordinate of V^0 primary vertex

both polarities (to correct for field effects) was analysed, a mis-alignment of 0.82 mm and 0.54 mm in the y and z direction respectively was found. This was corrected when reconstructing the beam trajectory by moving the track's y_0 and z_0 parameters.

4.7 Beam reconstruction efficiency

As mentioned before, for an estimation of the primary vertex, it is necessary for the beam to be reconstructed. Hence, all events where the beam was not reconstructed are discarded. A description of the hardware used in beam reconstruction is given in chapter 2.

The reconstruction procedure is similar to the reconstruction of ordinary tracks (telescope planes are used to compute the particle's track and a Runge-Kutta

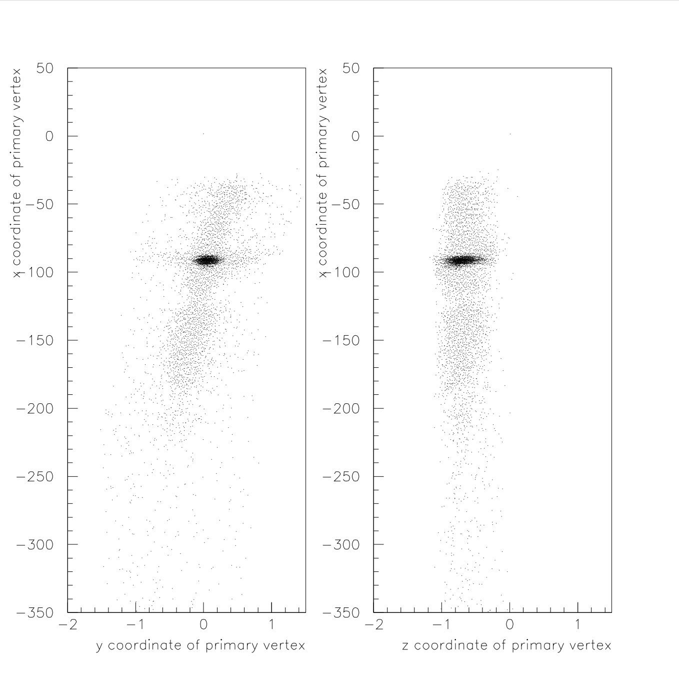

Figure 4.7: **Left:** x coordinate of primary vertex vs. z **Right:** x vs y

method is used to extend it). This section provides an estimate of it's efficiency. The most straight-forward method to get an estimate of the beam reconstruction efficiency is to count the number of events in a given run where the beam was reconstructed and divide it by the total number of events in that run. This procedure was performed on a sample of 30 runs, each containing about 10,400 events. The total efficiency over this range turned out to be 78 % with a variance of 3%.

However, this estimate was skewed by 5 runs with detector problems, during which the average efficiency was 0.4

Disregarding these 5 runs, the average efficiency is 86 %, with a variance smaller by 4 orders of magnitude. In the analysis described in the next chapter, an efficiency of 86 % was assumed and the data from the bad run numbers discarded.

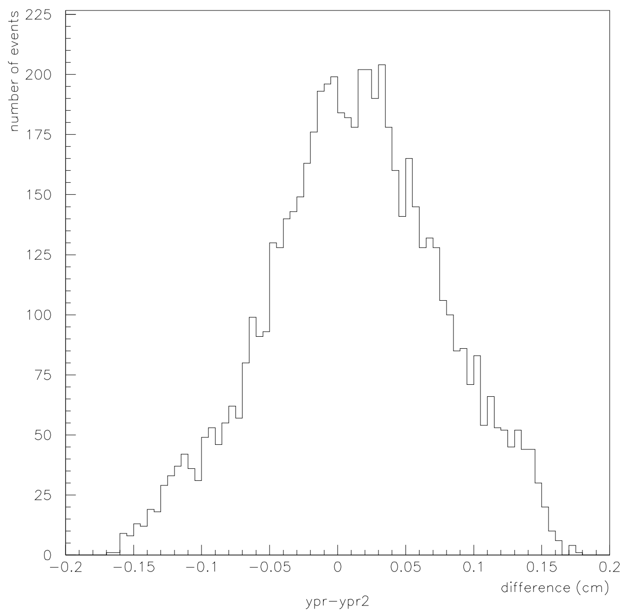

Figure 4.8: Difference between the two calculated values of the y-intersection point between beam and V^0 trajectory

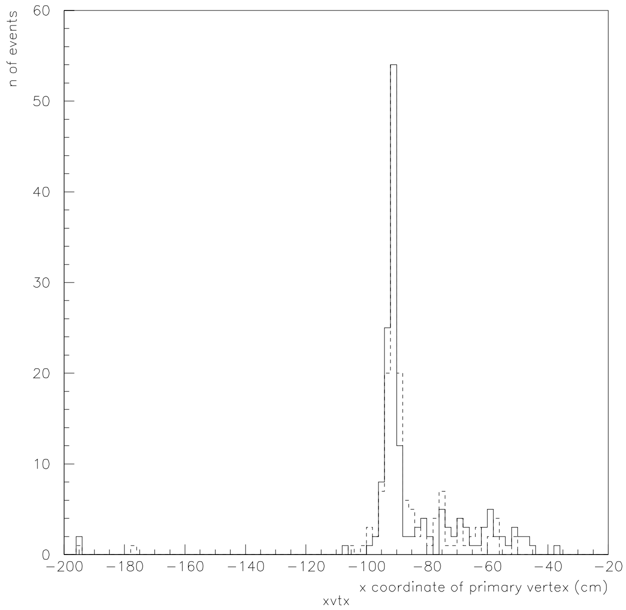

Figure 4.9: Analytical (solid line) and numerical (dotted line) x coordinate of the primary vertex

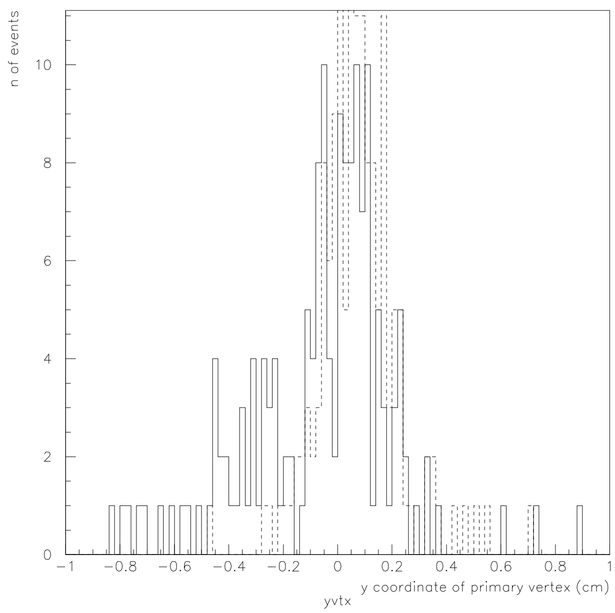

Figure 4.10: Analytical (solid line) and numerical (dotted line) y coordinate of the primary vertex

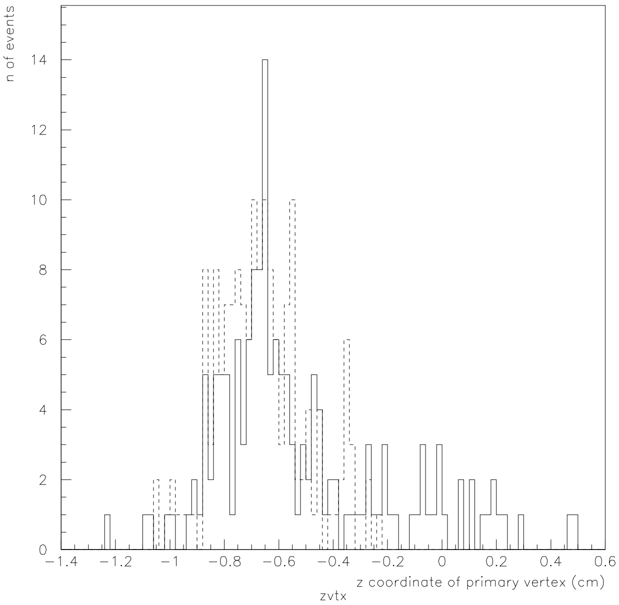

Figure 4.11: Analytical (solid line) and numerical (dotted line) z coordinate of the primary vertex

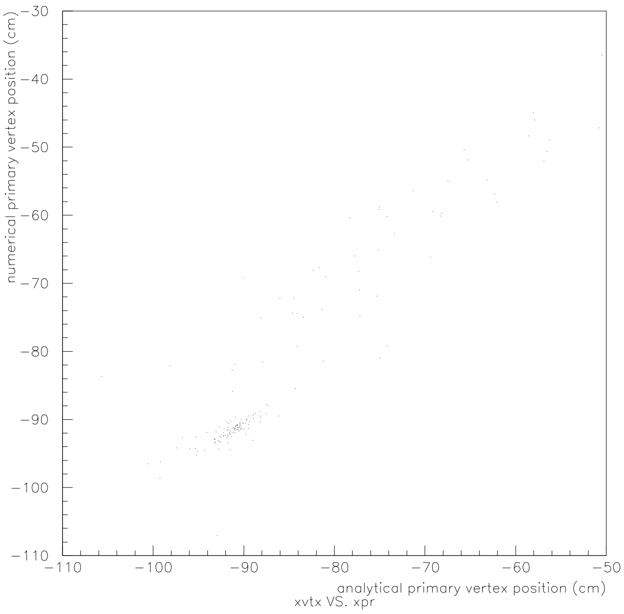

Figure 4.12: Analytical vs numerical calculation of x coordinate of π^- primary vertex

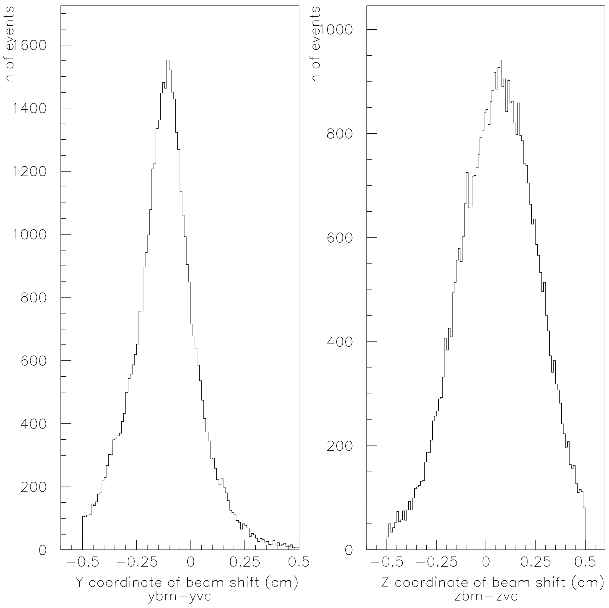

Figure 4.13: Left: $y_0 - y_{beam}$ Right:$z_0 - z_{beam}$

Chapter 5

Analysis of negatively charged particles

5.1 Introduction

As mentioned in chapter 1, in calculating strangeness enhancement, the hyperon yield can be normalised with the number of negative particles produced in the collision (referred henceforward as "negatives"). This chapter describes a procedure to estimate the latter and presents the results of its application to WA97 data. An m_T distribution for negative particles is also obtained and used to calculate the inverse slope for negative particles.

NB: In the analysis all tracks are assumed to be pions. Since $\frac{N_{pions}}{N_{kaons}} \approx 10$ this is a reasonable assumption.

5.2 Selection of negatives to be used in the analysis

5.2.1 Negatives from V^0 decays

Obviously, negatives coming from V^0 and cascade decays should not be used in this analysis. While the sample of background events used does not contain many V^0 s, the Armenteros plot in Fig. 5.1 shows some contamination of negatives from both Λ and K^0 decays (See the appendix and the preceding chapter for details on Armenteros plots). Therefore, all events with a V^0 topology have had the "mass" of the "neutral particle" reconstructed. For them to be considered further this mass has to differ from m_Λ and m_{K^0} as quoted in [33] by at least 30 Mev.

5.2.2 Primary Vertex

It was required that:

- both the analytical and the numerical procedure would have worked and given a result of a difference not less than 0.5 cm
- The closest approach distance between beam and particle should be not more than 0.5 cm
- This resulting primary vertex should be located between -96.6 cm and -86.6 cm. (The center of the target is at -91.6 cm).

The previous chapter gives the relevant distributions and describes the procedures used to obtain them in detail.

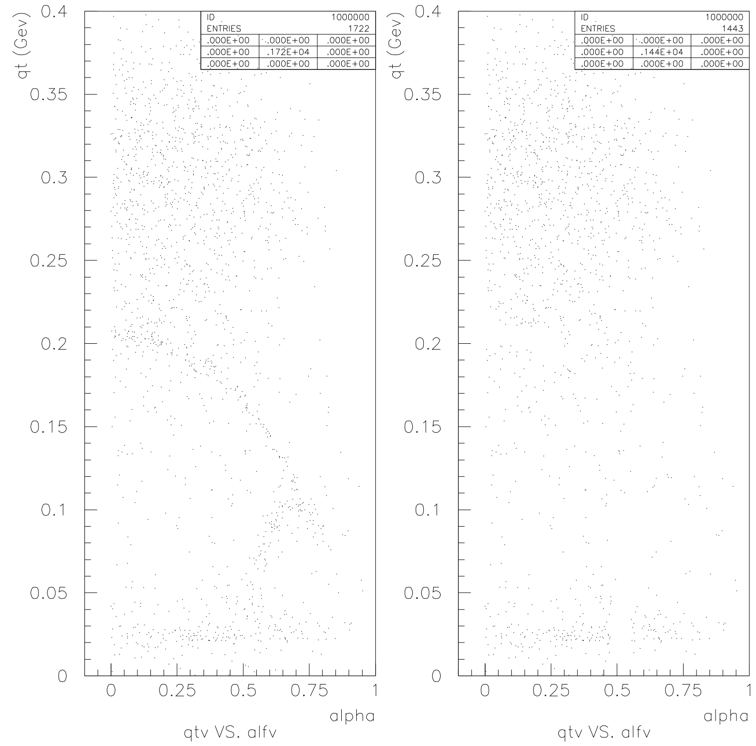

Figure 5.1: Left: "Armenteros plot" for events with both a negative and a positive track. As can be seen, a sizeable fraction of negatives on such events are part of Λ and K^0 decays. Right: Armenteros plot with the mass cuts. 12 % of V^0-type events are discarded

5.2.3 Impact parameter

Here, the impact parameter is defined as the distance between the x axis and the point of interaction at the plane $x = x_{interaction}$. Understandably, the impact parameter cut and the primary vertex cut significantly overlapped. Nevertheless, since an impact parameter larger than the beam spot radius is unphysical, an impact parameter cut was made on $|B| < 0.5$ cm (Fig. 5.2). As expected, very few events which passed the primary vertex cuts failed the impact parameter cuts.

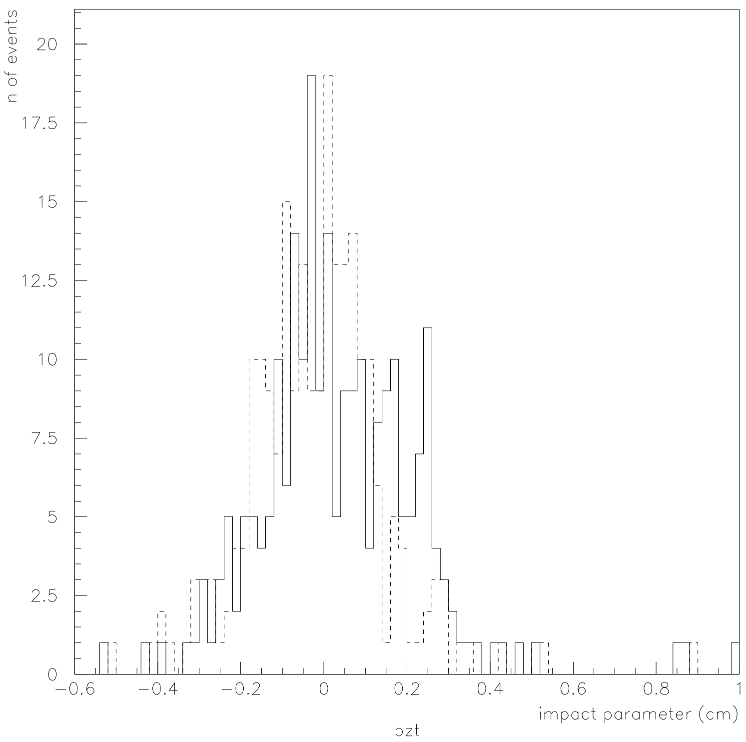

Figure 5.2: Impact parameter. Solid line: B_y, Dotted line B_z

5.2.4 Clean track cut

As illustrated in Fig. 2.4, there are 11 pixel planes complemented by 2 pairs of microstrip planes. The negative track can therefore have a maximum of 13 points. In order to ensure the analysed tracks are "clean", the minimum number of reconstructed points on the track was set at 7 and the track was required to pass through the first 4 consecutive pixel planes.

5.3 Final Sample

Fig. 5.3 shows a p_T-Y plot for the events which passed the cuts described above, inscribed in the p-Pb negatives acceptance window as calculated in [35]. While no calculation of the maximum and minimum of the angle the tracks make with respect to the beam was done before weighting the data, the agreement between the data and the published acceptance window is encouraging. Therefore it can be assumed a reliable sample for weight calculation has been obtained.

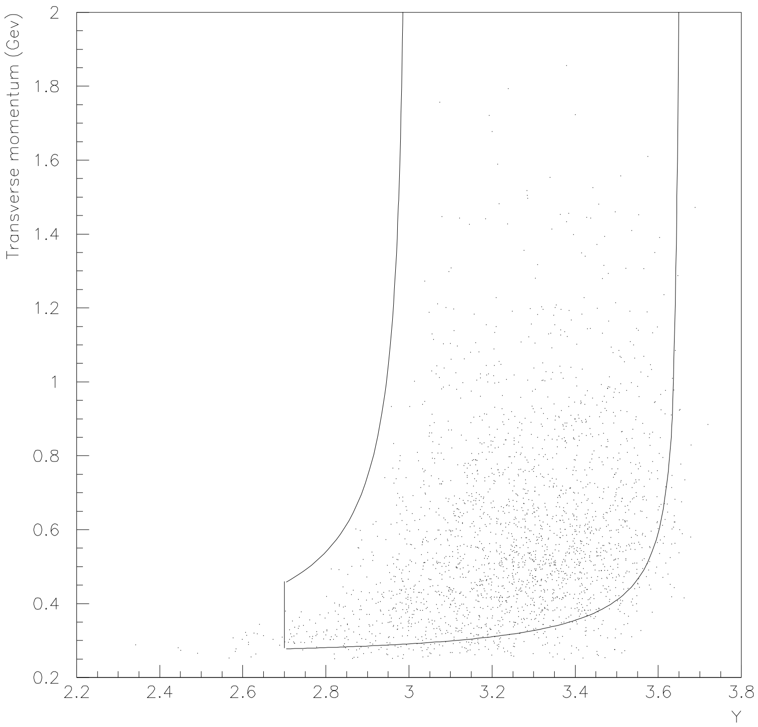

Figure 5.3: Y-p_T scatter plot of the data after cuts super-imposed with the acceptance window for negatives in p-Pb collisions [35]. This is slightly different from the p-Be acceptance region which will be decided in the next section. However, the overlap is a good sign that analysis so far is sound

5.4 Weights calculation

To use the sample obtained above in an analysis, it must be taken into account that the experiment does not have an 100% sensitivity and that its sensitivity to each event is different. Therefore, many tracks will not be correctly reconstructed and some spurious tracks will be reconstructed as real. In particular, a careful analysis must take account of:

- The geometrical acceptance, a measure of how the probability of the particle being detected depends on the geometry of the detector. As no decays are involved in a negative event, it is expected that the probability of the particle to be detected will be very close to 1 for particles emitted in the range of angles covered by the detector and 0 otherwise.
- The reconstruction efficiency. This is a measure of the efficiency of the various parts of the detector, as well as the track-finding efficiency of the off-line analysis software.

It was decided to find both efficiencies via a Monte carlo procedure (called weights chain) applied event by event, in which a sample of events having the same characteristics as a real event are generated, inserted into background files and reconstructed. The combined efficiency will then be given by the fraction of the sample which was correctly reconstructed. The inverse of the combined efficiency, referred to henceforward as the "weight" of the event, will be used in the analysis as the presumed number of undetected events with the same characteristics.

5.4.1 The weights chain

The following is a description of the weights chain. Fig 5.4 provides a diagram explaining each step.

- step 1

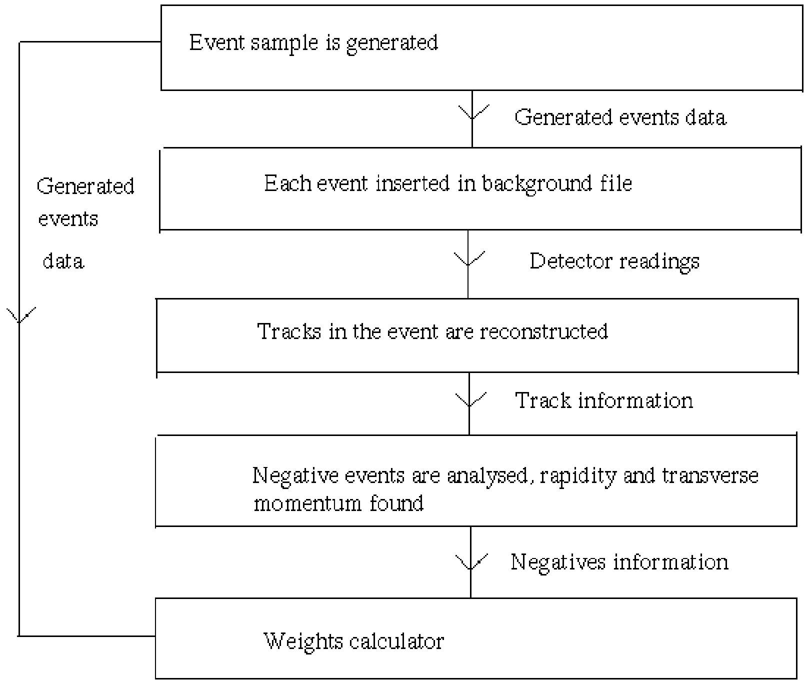

Figure 5.4: The weights chain

A sample of 5000 negative particles having the same rapidity and transverse momentum of each given event are generated. They are run through a Monte carlo simulator of the detector, which takes account of the electronic efficiency of each component, and measures how many telescope planes the track will pass through.

- step 2

  Each generated event will be inserted in a real background event of the same hits multiplicity as the original event and with a run number as close as possible to the original event's run number. It should be noted that, as Fig. 5.5 shows, the background file events will contain its own negative events. Care will be taken that it is the original events and not the background events, that will be reconstructed.

- step 3

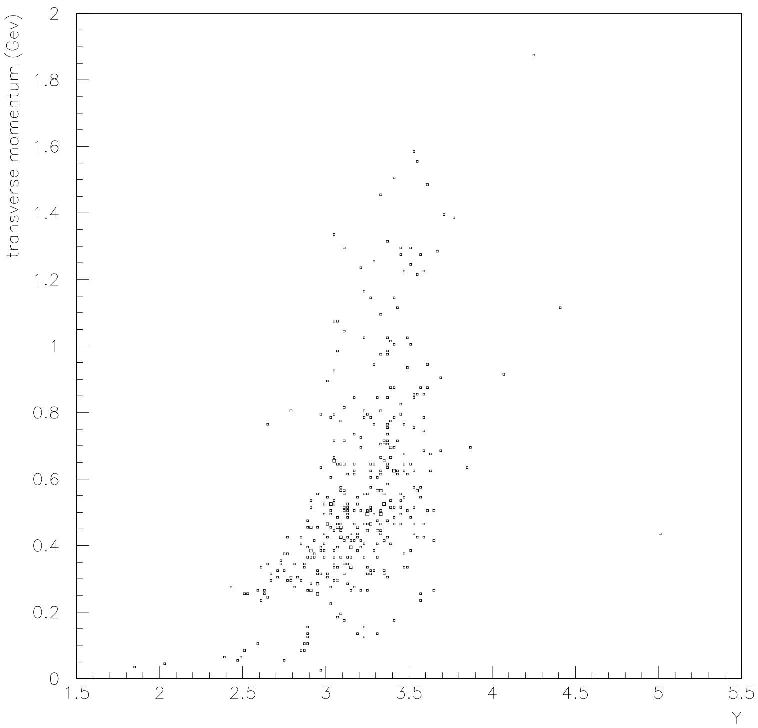

Figure 5.5: p_T - rapidity distribution of background events

The standard track-finding program is used to reconstruct the tracks from the detector readings.

- step 4

  The standard analysis program will be used to calculate the transverse momentum and rapidity of each reconstructed track. If each reconstructed event's transverse momentum and rapidity are within 0.2 Gev and 0.2 of the transverse momentum and rapidity of the original event, this event will be counted in the weighting.

- step 5

  The reconstructed tracks are compared with the generated tracks, and a weight is calculated.

A sample of 1500 events was weighted with the weights distribution shown in fig. 5.6. The value 20, around which the distribution is centered, is consistant with an acceptance dominated by the solid angle fraction of 4π covered by the detector.

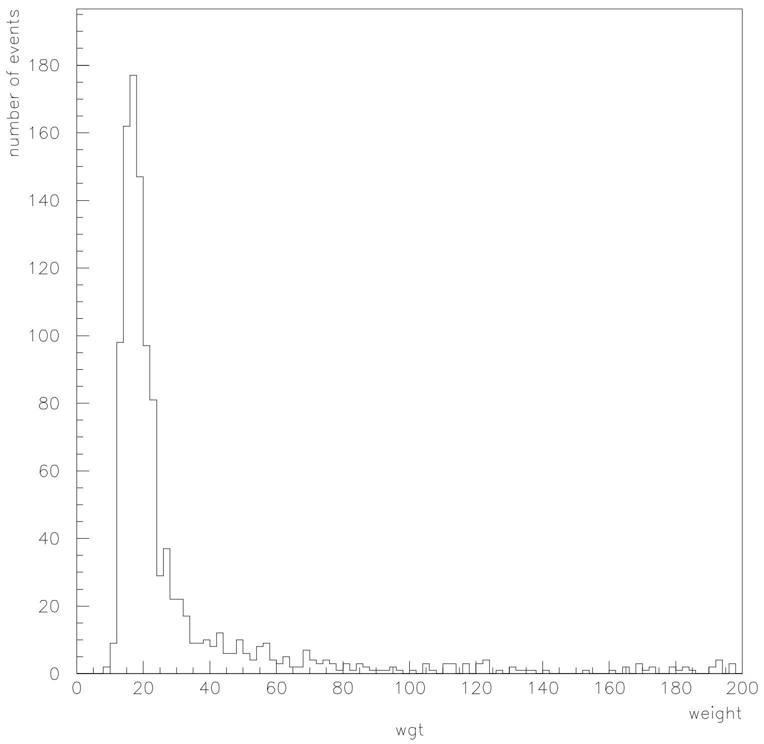

Figure 5.6: Weights distribution of negative events

5.5 Kinematic cuts

Before proceeding with the analysis, some further kinematic cuts have to be made to discard high-weight events for which the weighting procedure is unreliable. Some events, which "just" manage to pass through a corner of the detector, will not be simulated very reliably by the Monte carlo used in the weighting procedure. As the weight of such events will tend to be very high, their effect could be significant in the subsequent analysis. The way to compensate for this is to:

- Define a reliable acceptance region in the p_T rapidity plane where events tend to have sensible weights and only use events within this region for further analysis. Of course, there is no clear point where reliable weights become unreliable. However, as Figs 5.7, 5.8, 5.9 show, it is possible to eliminate most high-weight events by making cuts in rapidity, p_T and angle of flight with respect to the beam. It was decided, therefore, to consider as reliable those events with $3 < Y < 3.5, 0.5 < p_T < 2.5$ Gev/c (A constraint on the top and bottom corners of the acceptance window), $0.06 < \theta < 0.1$ (a constraint on the curvilinear boundaries).

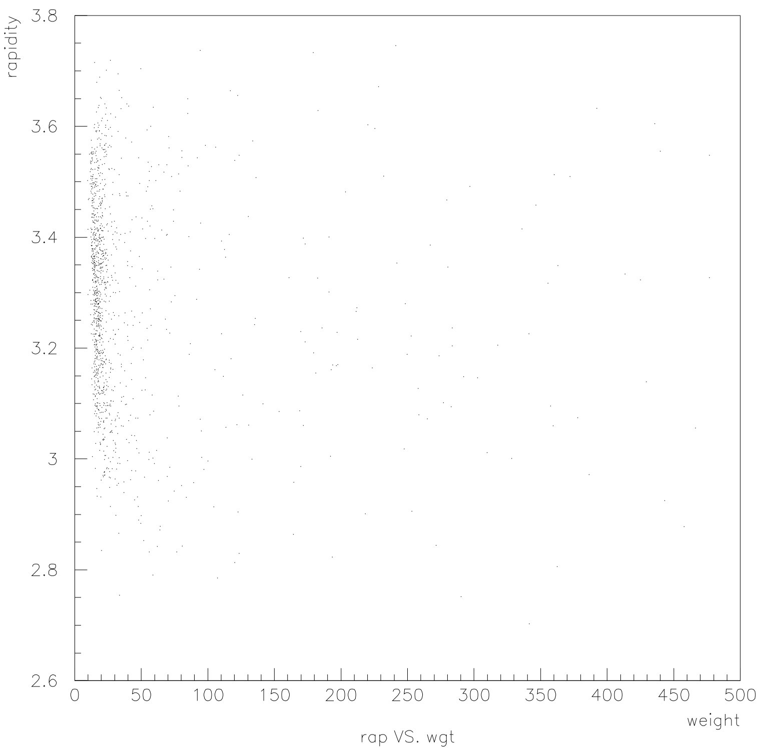

Figure 5.7: Dependence of weights on rapidity

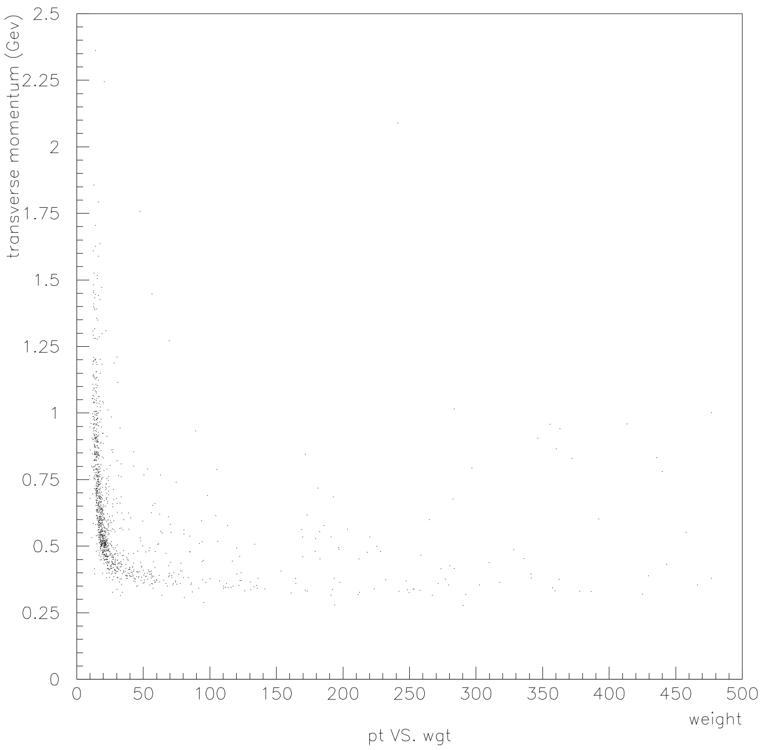

Figure 5.8: Dependence of weights on p_T

- Directly cut events with abnormal weights from the sample. This should be used only for blatantly unrealistic events whose weights were due to obvious computing problems, as arbitrarily limits on weights can very easily be turned into massaging of data to artificially deselect events which give the "wrong" result. In this analysis, events with a weight bigger than 1000 (100 times bigger than the smallest weight) have not been considered.

The final acceptance region is shown in Fig. 5.10

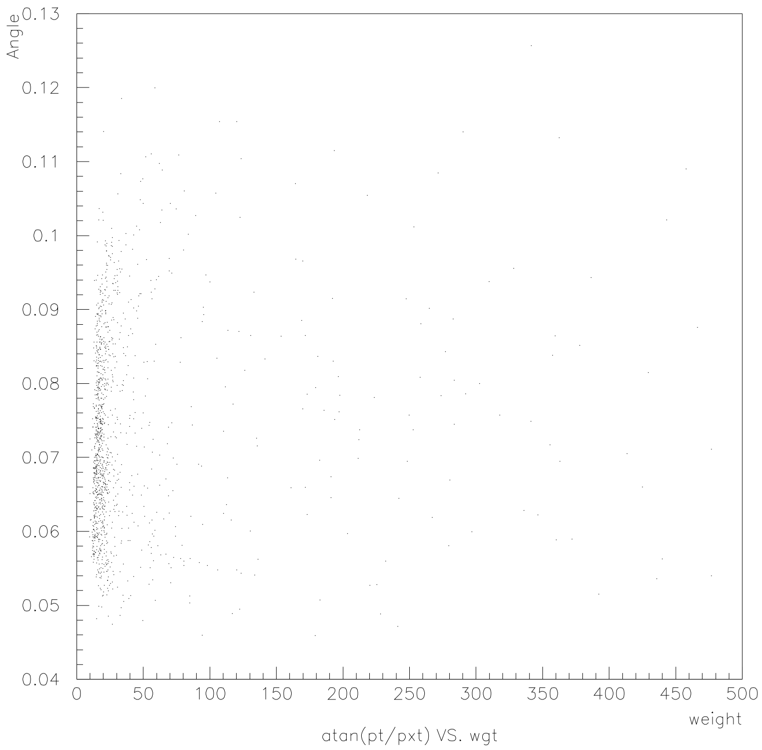

Figure 5.9: Dependence of weights on θ

5.6 Results

5.6.1 Inverse slope

The sample of weighted events was fitted to $\frac{dN}{dm_T} = f(y) m_T^{\alpha} e^{-\frac{m_T}{T}}$, where $f(y)$ was assumed to be a constant and $\alpha = 1$ (consistent with small acceptance experiments). The fit was performed using the method of maximum likelihood, taking into account the non-rectangular shape of the acceptance window. The T parameter was found to be 187.5 ± 6.4 Mev and a logarithmic plot of $\frac{1}{m_T}\frac{dN}{dm_T}$ against m_T is shown in Fig. 5.11

For comparison the inverse slopes for each particle are provided in Table 5.1 [35] , [37].

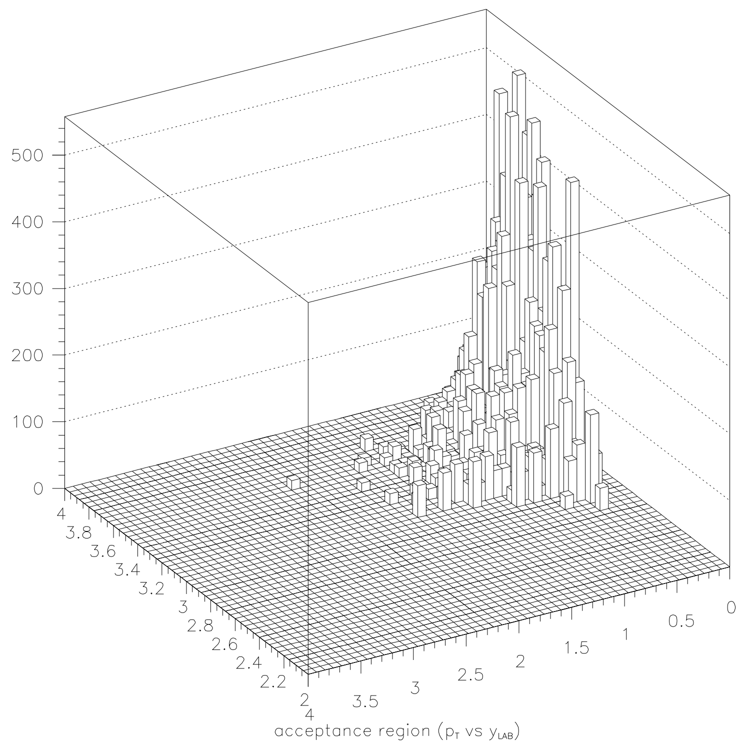

Figure 5.10: Rapidity and p_T distribution of weighted events

Overall, inverse slopes seem to rise with heavier collisions. Whether this is more due to increased temperature or transverse flow is unclear. It should also be remembered that, because of the transverse flow component, the inverse slope depends strongly on the particle's cross-sectional area with other particles present in the fireball (and those particle's relative abundance).

5.6.2 Negatives Yield

Once the T parameter is found, the data sample used in the weighting can be extrapolated to find the total number of negative particles produced in the rapidity region used by WA97. To do this, a flat central rapidity region is assumed and $\frac{dN}{dm_T}$ is integrated with respect to m_T. The rapidity region to

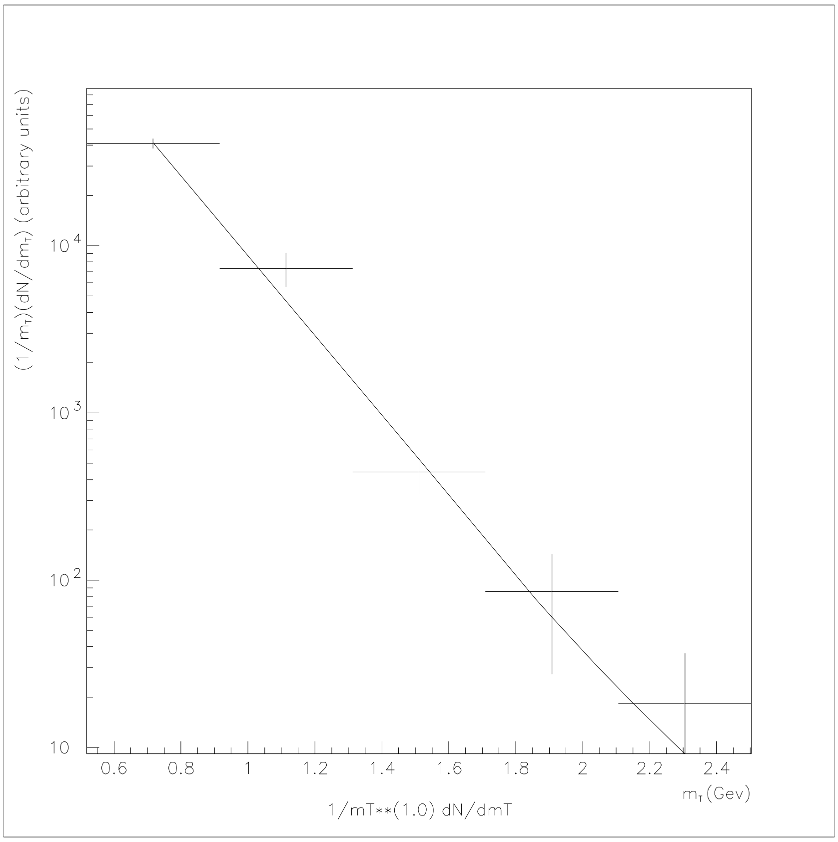

Figure 5.11: Inverse slope for negatives

which the data is extrapolated is $2.42 < Y < 3.42$ (the same as for Pb-Pb) and the integration over $m_{\pi^-} < m_T < \infty$ results in a total of 118536.9 ± 10568.5 negatives.

To obtain the yield, the number of negatives has to be normalised by the total number of interactions and the beam reconstruction efficiency. The number of interactions is estimated at 151800 using the online processing records of the considered events. The beam reconstruction efficiency, as calculated in the previous chapter, is 86%. Hence, the total normalising factor is 182600 and the negatives yield is 0.93 ± 0.08.

Table 5.1: Inverse slopes (in units of MeV) with $\alpha = 1$.

	p-Be	p-Pb	Pb-Pb
h^-	187.5 ± 6.4	185 ± 5	213 ± 8
Λ	180 ± 3	203 ± 9	291 ± 18
$\overline{\Lambda}$	157 ± 2	180 ± 15	280 ± 20
Ξ^-	202 ± 13	235 ± 14	286 ± 9
$\overline{\Xi}^+$	182 ± 17	224 ± 21	284 ± 17
$\Omega^- + \overline{\Omega}^+$	169 ± 40	334 ± 99	251 ± 19

Chapter 6

Conclusions and outlook

6.1 Strangeness enhancement

The weighting and extrapolation procedure similar to that described in the previous chapter has been applied to the full sample of Ξ s and Ω s and a representative sample of Λ s in p-Be, p-Pb and Pb-Pb events. The yields for negatives and hyperons normalised to the number of interactions for control (p-Pb and p-Be) events are included in table 6.1, while table 6.2 gives the yields for Pb-Pb interactions [38]. The latter are divided in 4 bins according to the charged particle multiplicity, which is a measure of the centrality of the collision [26] (The multiplicity boundaries and relative abundancies of the bins are shown in Fig. 6.1).

Any quantity which does not depend on strangeness can reasonably be used for normalisation. In this study, the data has been correlated both with the negatives production (Fig. 6.2) and the number of participants. (Fig. 6.3).

Both these quantities were then used to calculate the enhancement, defined as $(\frac{Y}{N}_{Pb-Pb})/(\frac{Y}{N}_{p-Be})$, where Y is the yield and N is the normalisation constant. The enhancement normalised to the negatives yield is shown in table 6.3 and

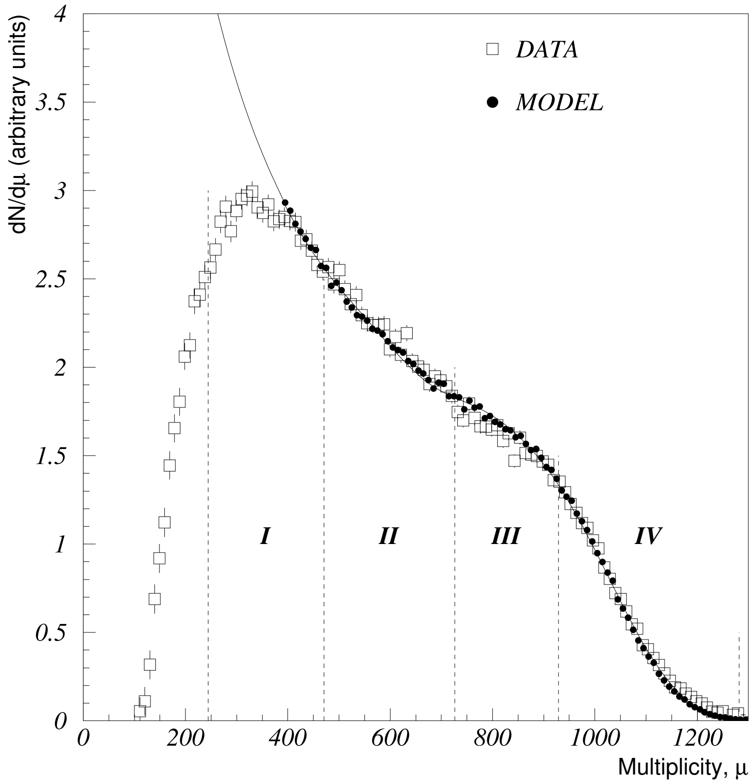

Figure 6.1: Distribution of the particle multiplicity of the data superimposed on a Glauber distribution. In the Glauber model, the centrality is assumed to be proportional to the multiplicity, with a Poisson deviation. The constant of proportionality, dependant on the acceptance, is fitted from the multiplicity distribution: Maximum multiplicity events are assumed to have had as active participants all the nucleons in the colliding ions (300 participants), while obviously no participants corresponds to zero multiplicity.

Figs 6.4 (particles), 6.5 (antiparticles). Table 6.4 and Figs 6.6 , 6.7 show the enhancement normalised to the number of participants. It is immediately clear that normalizing by the number of participants makes the enhancement and its increase with hyperon strangeness content more apparent. Indeed, it turns out that there is actually a suppression of $\overline{\Lambda}$ s with respect to negatives production. The reason for this suppression is that anti-baryons can interact inelastically in a baryon-rich medium with relative ease (much more easily than mesons do). At high baryon density (such as in a lead-lead fireball) this can compensate

Table 6.1: Yields of control events measured by the WA97 experiment

Proton data:	p-Be	p-Pb
π^-	0.93 ± 0.08	1.26 ± 0.19
Λ	0.033 ± 5.92E-4	0.060 ± 0.002
$\overline{\Lambda}$	0.011 ± 2.04E-4	0.015 ± 0.001
Total Λ	0.046 ± 5.99E-4	0.075 ± 0.0025
Ξ	0.0015 ± 0.0001	0.0030 ± 0.0002
$\overline{\Xi}$	0.00068 ± 0.0001	0.0012 ± 0.0001
Total Ξ	0.0021 ± 0.0002	0.0042 ± 0.0003
Ω	1.2E-4 ± 0.6E-4	2.22E-4 ± 0.8E-4
$\overline{\Omega}$	3.9E-5 ± 2.1E-5	4.67E-5 ± 2.5E-5
Total Ω	1.6E-4 ± 0.6E-4	2.63E-4 ± 0.78E-4

for the strangeness enhancement and even overturn the slight enhancement of $\overline{\Lambda}$ production (similar reasons can also explain the peculiar shape of the Ω enhancement distribution). Because of this effect, and because there are other factors of interest (such as entropy increase) which influence negatives multiplicity, the negatives yield is not as good a normalisation parameter as the number of participants.

In addition, a slight enhancement of all strange hyperons is observed in the p-Pb collision. As can be seen from 6.6 and 6.7, it actually corresponds to a drop in negatives production. This can be accounted for by fact that the p-Pb collision is a lot more asymmetrical than either the p-Be and Pb-Pb collisions. The rapidity distribution of particles produced in the interaction, therefore, is different (and the effect varies according to particle type). As explained in chapter 2, this is the main reason of having the p-Be run in the first place.

Comparing this data with the earlier p-Pb-normalised enhancements (given in the last section of chapter 1), it is clear that p-Be control events confirm the

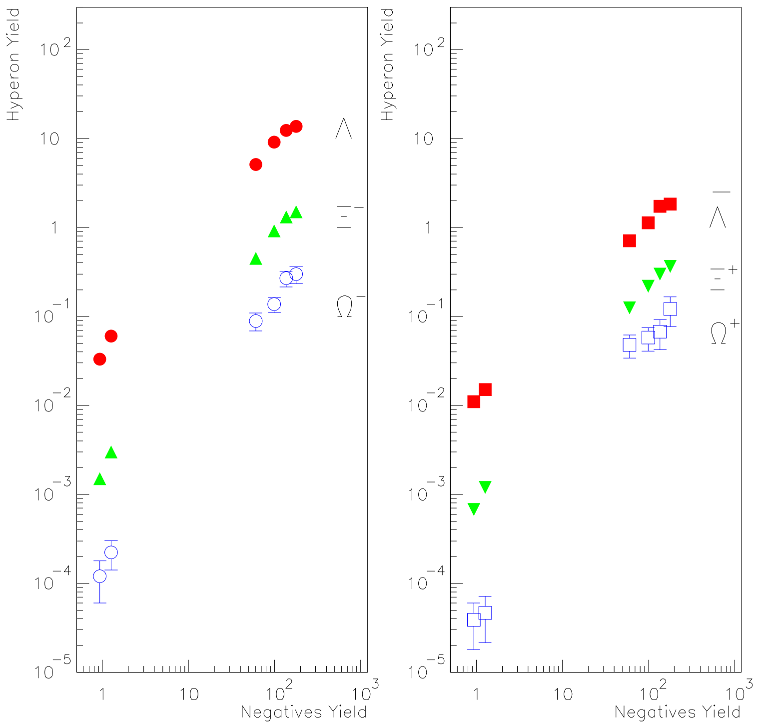

Figure 6.2: Hyperon yields plotted against negative yields

earlier results obtained by the WA97 experiment. A strangeness enhancement is seen and, in general, hyperons with a greater strangeness content are significantly more enhanced. Thus, this data is explained very well by the QGP model. It is not enough, however, to eliminate the hadron gas model completely, since, as seen in chapter 1, it can also explain the elevated strangeness production (although, taken in conjunction with the evidence of charmonium suppression and meson mass shifts, it is very plausible that at least partial QGP formation has occurred). Further measurements are possible, however, which would put more constraints on the model and allow us to test the viability of the QGP and HG models further.

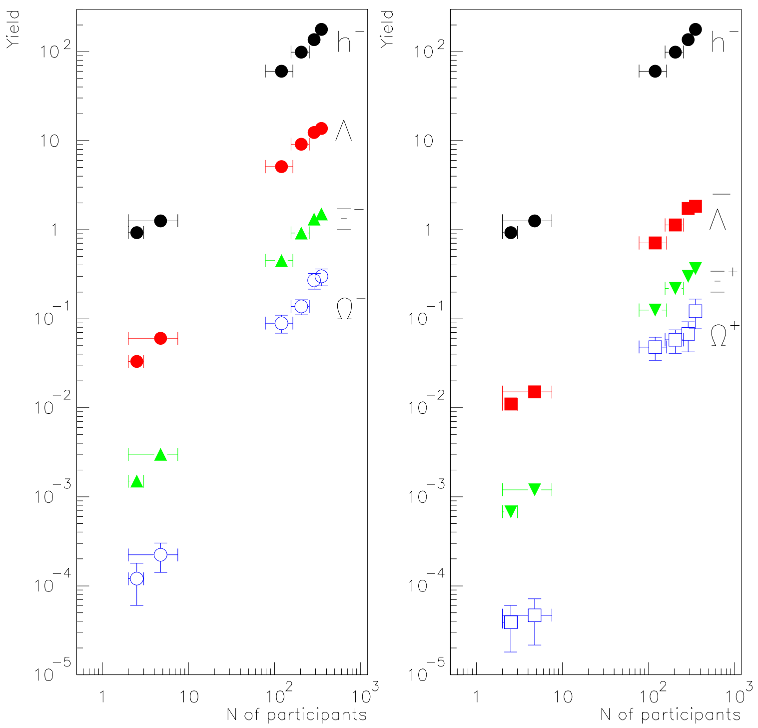

Figure 6.3: Hyperon and negative yields plotted against centrality

6.2 Future heavy ion physics experiments

At present, it is possible to measure the chemical potentials (from the hyperon ratios) and the temperature (from a fit to m_T). However, it is obvious that the entropy per strange particle in a hadron gas is significantly different than that of a quark gluon plasma. (The QGP should produce a greater amount of entropy since there are many more degrees of freedom). Measuring the entropy per baryon in the system could very well be crucial in determining the system's state. Another way to constrain the observed data is to explore how enhancement increases with the temperature: does it suddently arise when a critical energy is reached, or is it more like a continuous growth? The NA57 experiment (described in more detail in chapter 2) was planned to do both these

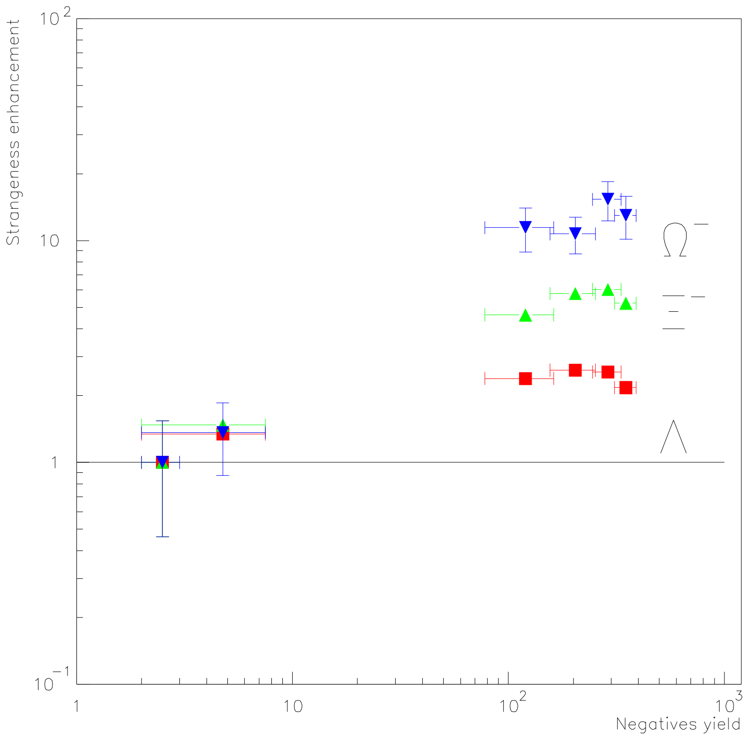

Figure 6.4: Strangeness enhancement of particles normalised by negatives yield

measurements at the WA97 baryon density. Data from its particle multiplicity measurements and its lower energy run might be able to ascertain whether the SPS has already obtained a partial QGP. (However, it is now doubtful that the entropy measurement will be performed since the pixel multiplicity detectors have not been built).

After NA57, the use of colliders rather than fixed target experiments will permit a much greater increase in the attainable fireball temperature. The first experiments of this kind will be based in the Relativistic Heavy Ion Collider in Brookheaven, colliding gold ions together. The RHIC-based experiments will look for both hard probes, such as jet quenching and charmonium suppression, and strangeness enhancement.

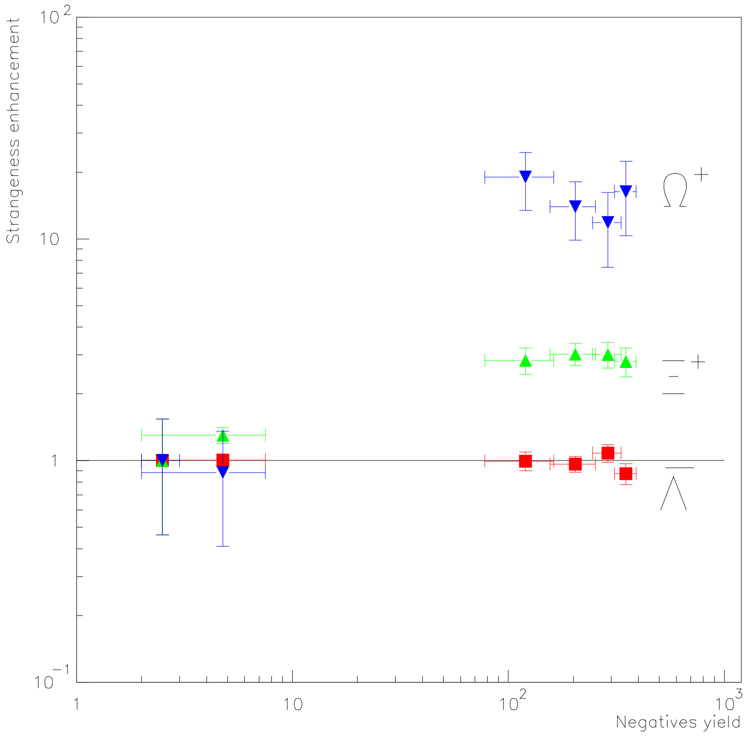

Figure 6.5: Strangeness enhancement of antiparticles normalised by negatives yield

However, in the long term the definitive results in the field might be provided by the ALICE experiment, in CERN's Large Hadron Collider. Because of the enormous LHC energies (7 Tev/nucleon) it is expected that a full lead-lead collision will produce a pure QGP state. However, as ALICE can also work with p-p and lighter ion collisions, it will be able to explore the entire phase diagram of hadronic matter, from a pure HG to a mixed phase and the pure QGP phase ,by varying the type of collision studied. ALICE will also be the first experiment to look at a whole range of signatures, including dileptons to measure chiral symmetry restoration , quarkonium (both charmonium and bottomonium) suppression to probe the QGP phase directly and direct photons to

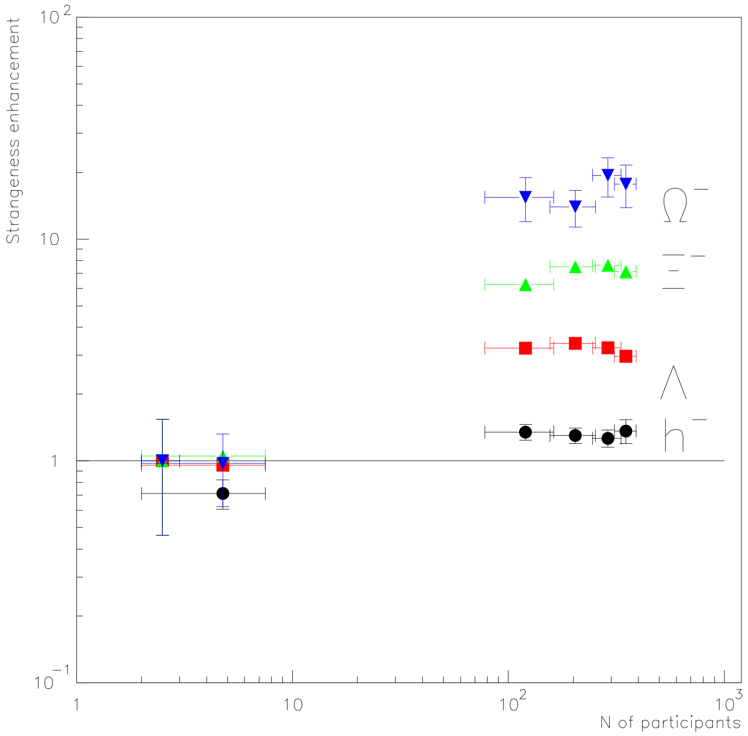

Figure 6.6: Strangeness enhancement of particles normalised by the number of participants

constrain the thermodynamic state of the system. Strangeness enhancement will be further explored by measurement of hyperon production, the K/π ratio, and rare strange mesons such as Φ (indicative of the time-scale for strangeness equilibration). Strangelets (exotic many-quark states) will also be looked for. Because of the high multiplicity in a typical ALICE collision, and ALICE's wide acceptance region, it will be possible to perform several measurements on an event-by-event basis, since a typical heavy ion event will produce enough particles of the same type to form a reliable signal.

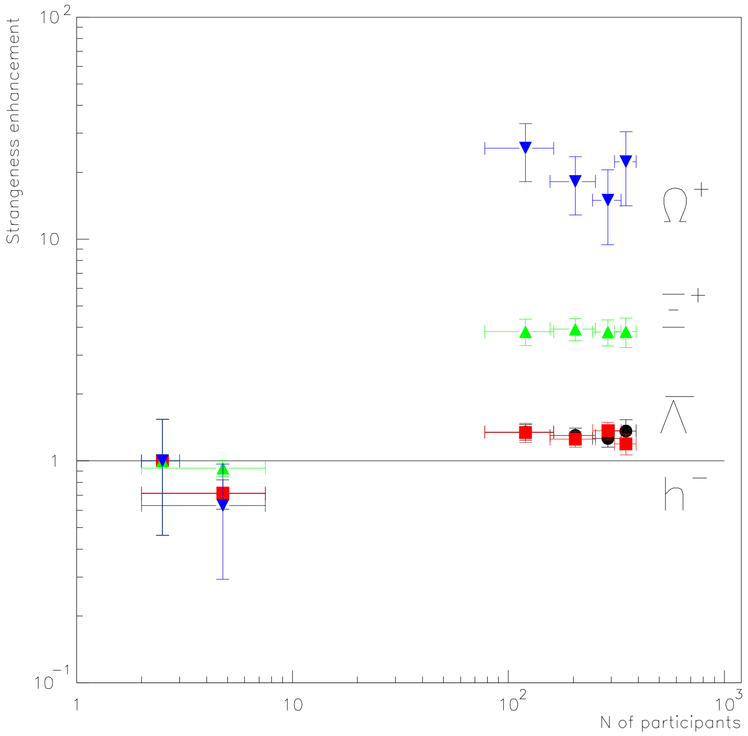

Figure 6.7: Strangeness enhancement of antiparticles normalised by the number of participants

6.3 conclusion

The WA97 experiment took measurements of the yield of all strange hyperons and anti hyperons. For the first time Ω and $\overline{\Omega}$ statistics have been collected, and statistics for Ξ, Λ, K^0 has been greatly expanded. The results seem to confirm many of the predictions of the QGP model: A marked enhancement of strange hyperons yields has been observed, and found to increase with strangeness content. While a rock-solid confirmation of QGP production has not been achieved yet, the results definitely look promising and strongly invite further measurements to ascertain whether QGP has been formed. It is hoped future heavy ions experiments will achieve this.

Table 6.2: Yields of Pb-Pb events measured by the WA97 experiment

Pb-Pb data:	Bin 1	Bin 2
No. of Participants	120.1 +37.4 -42.3	204.6 +41.4 -48.9
π^-	60.3 $\pm$ 5.0	99.0 $\pm$ 8.0
Λ	5.11 $\pm$ 0.29	9.15 $\pm$ 0.43
$\overline{\Lambda}$	0.71 $\pm$ 0.069	1.13 $\pm$ 0.092
Total Λ	5.82 $\pm$ 0.30	10.29 $\pm$ 0.446
Ξ	0.45 $\pm$ 0.03	0.92 $\pm$ 0.05
$\overline{\Xi}$	0.125 $\pm$ 0.017	0.219 $\pm$ 0.025
Total Ξ	0.576 $\pm$ 0.038	1.14 $\pm$ 0.060
Ω	8.9E-2 $\pm$ 2.0E-2	0.137 $\pm$ 2.6E-2
$\overline{\Omega}$	4.8E-2 $\pm$ 1.4E-2	5.8E-2 $\pm$ 1.7E-2
Total Ω	0.133 $\pm$ 2.39E-2	0.189 $\pm$ 3.02E-2
Pb-Pb data	Bin 3	Bin 4
No. of Part.	289.0 +38.0 -43.3	350.6 +40.7 -31.4
π^-	36.0 $\pm$ 12.0	178.0 $\pm$ 22.0
Λ	12.33 $\pm$ 0.67	13.74 $\pm$ 0.89
$\overline{\Lambda}$	1.74 $\pm$ 0.16	1.84 $\pm$ 0.20
Total Λ	14.1 $\pm$ 0.695	15.6 $\pm$ 0.92
Ξ	1.32 $\pm$ 0.08	1.5 $\pm$ 0.1
$\overline{\Xi}$	0.2997 $\pm$ 0.040	0.365 $\pm$ 0.055
Total Ξ	1.62 $\pm$ 0.094	1.82 $\pm$ 0.13
Ω	0.269 $\pm$ 5.4E-2	0.298 $\pm$ 6.5E-2
$\overline{\Omega}$	6.75E-2 $\pm$ 2.5E-2	0.122 $\pm$ 4.49E-2
Total Ω	0.324 $\pm$ 5.72E-2	0.408 $\pm$ 7.69E-2

Table 6.3: Strange hyperon enhancements with respect to proton-beryllium data normalised using negatives yields

Particle	p-Pb	Bin 1	Bin 2	Bin 3	Bin 4
Λ	$.96 \pm .15$	$1.71 \pm .17$	$1.87 \pm .17$	$1.83 \pm .19$	$1.56 \pm .22$
$\overline{\Lambda}$	$1.01 \pm .17$	$1.00 \pm .13$	$.97 \pm .11$	$1.08 \pm .14$	$.87 \pm .14$
Ξ	$1.48 \pm .24$	$4.63 \pm .49$	$5.76 \pm .56$	$6.02 \pm .64$	$5.22 \pm .73$
$\overline{\Xi}$	$1.30 \pm .22$	$2.84 \pm .45$	$3.03 \pm .42$	$3.01 \pm .48$	$2.80 \pm .55$
Ω	$1.37 \pm .53$	11.44 ± 2.74	10.72 ± 2.21	15.33 ± 3.36	12.97 ± 3.25
$\overline{\Omega}$	$.88 \pm .49$	18.98 ± 5.76	13.97 ± 4.25	11.84 ± 4.51	16.34 ± 6.35

Table 6.4: Strange hyperon enhancements with respect to proton-beryllium data normalised using the number of participants

Particle	p-Pb	Bin 1	Bin 2	Bin 3	Bin 4
Λ	$.71 \pm .43$	$1.35 \pm .49$	$1.30 \pm .33$	$1.27 \pm .22$	$1.36 \pm .21$
$\overline{\Lambda}$	$.69 \pm .40$	$2.31 \pm .82$	$2.43 \pm .59$	$2.32 \pm .37$	$2.13 \pm .24$
Ξ	$.72 \pm .42$	$1.34 \pm .49$	$1.26 \pm .32$	$1.37 \pm .24$	$1.19 \pm .17$
$\overline{\Xi}$	$1.05 \pm .61$	6.24 ± 2.24	7.49 ± 1.84	7.61 ± 1.23	$7.13 \pm .80$
Ω	$.93 \pm .54$	3.83 ± 1.44	3.94 ± 1.04	$3.81 \pm .77$	$3.83 \pm .67$
$\overline{\Omega}$	$.97 \pm .66$	15.44 ± 6.45	13.95 ± 4.26	19.39 ± 4.86	17.71 ± 4.18
π^-	$.63 \pm .50$	25.62 ± 11.72	18.17 ± 6.87	14.97 ± 5.98	22.31 ± 8.45

Appendix A

Appendix 1: Armenteros-Podolanski plots

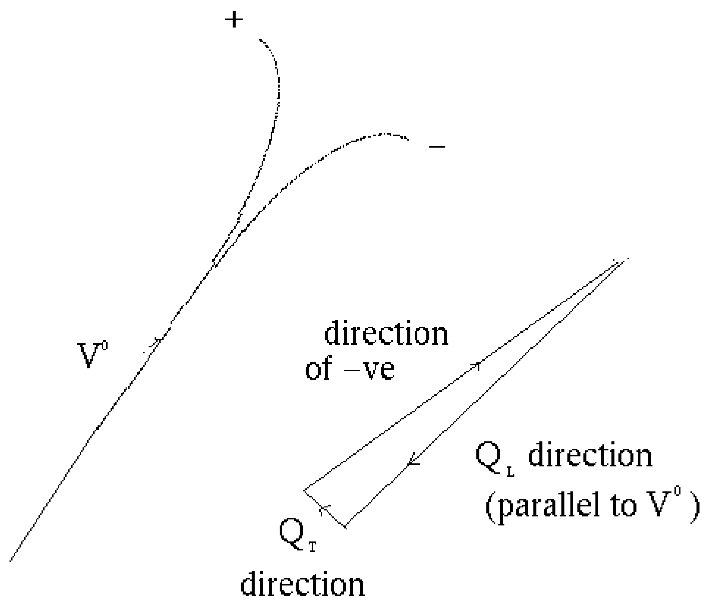

Figure A.1: Decay of a neutral particle into two components

Armenteros-Podolanski plots provide a very useful tool to analyse the decay of a particle (a) into two tracks (called here + and -). This appendix gives a proof that in the q_T - α plane, such events will fall into elliptical loci. Here q_T is the transverse component of momentum of particle a $\alpha = \frac{q_L^+ - q_L^-}{q_L^+ + q_L^-}$. where $q_L^{\pm}$ are the longitudinal components of the momenta of $q^{\pm}$

Let (a) have velocity β with respect to the lab frame.

In (a)'s rest frame (all quantities in (a)'s rest frame denoted by an asterisk):

$$q_{L+}^* = |q^*|cos(\theta^*) \tag{A.1}$$

$$q_{T+}^* = |q^*|sin(\theta^*) \tag{A.2}$$

$$E_+^* = \sqrt{|q^{*2}| + m_+^2} \tag{A.3}$$

In the lab frame:

$$E_+^{lab} = \gamma E_+^* + \beta\gamma q_{L+}^* \tag{A.4}$$

$$q_{L+}^{lab} = \gamma q_{L+}^* + \beta\gamma E_+^* = \gamma|q^*|cos(\theta^*) + \beta\gamma E_+^* \tag{A.5}$$

$$q_{T+}^{lab} = q_{T+}^* = |q^*|sin(\theta^*) \tag{A.6}$$

and, as $q_{L-}^* = -q_{L+}^*$

$$q_{L-}^{lab} = -\gamma|q^*|cos(\theta^*) + \beta\gamma E_-^*(b) \tag{A.7}$$

Hence by subtracting (6.7) from (6.5)

$$q_{L+}^{lab} - q_{L-}^{lab} = 2\gamma\| q^*|cos(\theta) + \beta\gamma(E_+^* + E_-^*) \tag{A.8}$$

and by conservation of momentum

$$q_{L+}^{lab} + q_{L-}^{lab} = q_a^{lab} = \beta\gamma m_a \tag{A.9}$$

Therefore, by definition of α and dividing (6.8) over (6.9)

$$\alpha = \kappa cos(\theta^*) + \lambda \tag{A.10}$$

where $\kappa = \frac{2|q^*|}{\beta m_a}$, $\lambda = \frac{E_+^* - E_-^*}{m_a}$

$$cos(\theta^*) = \frac{\alpha - \lambda}{\kappa} \tag{A.11}$$

$$sin(\theta^*) = \frac{q_T^+}{|q^*|} \tag{A.12}$$

As $cos^2(\theta^*) + sin^2(\theta^*) = 1$

$$(\frac{\alpha - \lambda}{\kappa})^2 + (\frac{q_T^*}{|q^*|})^2 = 1 \tag{A.13}$$

Which is the formula for an ellipse, with semiaxes $\frac{2q^*}{\beta m_a}$ and q^*, and center $(\lambda, 0)$

As a factor β appears in the ellipse parameters, it is not relativistically invariant. However, as in practice $\beta \simeq 1$ the invariance can be neglected.

Appendix B

Appendix 2: Acceptance windows shapes

For both theoretical and experimental reasons, it is convenient to parametrize the direction of the outgoing particles by the component of the momentum transverse to the beam p_T and the rapidity $Y = \frac{1}{2}ln(\frac{E+p_L}{E-p_L})$, where E is the energy and p_L is the longitudinal component of momentum. The two quantities depend on the particle mass ,it's direction and it's total momentum. Their relationship, however, is not immediately apparent and it's derivation is somewhat laborious. Because the peculiar shape of the WA97 acceptance windows is a direct consequence of this relationship, this appendix provides an outline of the derivation. Rearranging the expression for Y,

$$e^{2Y} = \frac{E + p_L}{E - p_L} \tag{B.1}$$

Solving for p_L

$$p_L = E\frac{e^{2Y} - 1}{e^{2Y} + 1} \tag{B.2}$$

Now, $\frac{e^{2Y}-1}{e^{2Y}+1} = \frac{e^{Y}-e^{-Y}}{e^{-Y}+e^{Y}}\frac{e^{Y}}{e^{Y}} = tanh(Y)$.

Hence,

$$p_L^2 = E^2 tanh^2(Y) \tag{B.3}$$

By hyperbolic relations,

$$\frac{1}{tanh^2(Y)} = 1 + \frac{1}{sinh^2(Y)} \tag{B.4}$$

and B.3 can be rewritten as

$$E^2 - p_L^2 = p_L^2 \frac{1}{sinh^2(Y)} \tag{B.5}$$

However, considering that

$$E^2 = p_L^2 + p_T^2 + m^2 \tag{B.6}$$

it is possible to rewrite B.5 in terms of $p_{L,T}$ and m:

$$p_L^2 = (p_T^2 + m^2) sinh^2(Y) \tag{B.7}$$

Finally, the geometrical relationship between p_T and p_L is

$$p_T = P_L \frac{sin(\theta)}{cos(\theta)} \tag{B.8}$$

where θ is the angle between the direction of the particle and the beam. Putting B.8 into B.7 and solving for p_T will yield to the y-p_T relationship

$$P_T = \frac{msinh(Y)sin(\theta)}{\sqrt{cos(\theta)^2 - sin(\theta)^2 sinh(Y)^2}} \tag{B.9}$$

.

Hence, if the detector covers a limited range of angles with respect to the beam, the acceptance region for a particular particle will assume the characteristic curved shape. The 2 curves delimiting it will correspond to the maximum and minimum angles covered by the detector.

Bibliography

[1] Berndt Muller Physics and Signatures of the Quark-Gluon plasma , Review article for Progress in physics, 4 oct 1994, DUKE TH 94-76 (nucl-th/9410005)

[2] Berndt Muller Probing the fifth state of matter with Relativistic heavy ions: A theoretical overview 14th International Conference on Particles and Nuclei : PANIC '96 Williamsburg, VA NUCL-TH-9410005

[3] John W Harris and Berndt Muller Quark-Gluon Plasma search Annual Review Nuclear and Particle Science 1996 Preprint DUKE TH 96-105 (hep-ph/9602235)

[4] Heavy ion collisions at the LHC, J Paic 3th International Conference on Physics and Astrophysics of Quark Gluon Plasma (ICPAQGP '97), Jaipur, India, 17-21 March, 1997.

[5] S. Drell and T.M.Yan, Phys. Rev. Lett. 25 316 (1970).

[6] M.C. Abreu et al , Charmonium production at 450 Gev/c proton induced reactions , Phys. Lett. B 444 (1998) 516-522

[7] M.C. Abreu et al, Observation of a threshold effect in the anomalous J/psi suppression Physics letters B 450(1990) 456-466

[8] Deconfinement and chiral symmetry restoration, Frithjof Karsch, hep-lat/9903031

[9] Low mass e^+e^- pair production in 158 GeV Pb-Au collisions at the CERN SPS, its dependence on multiplicity and transverse momentum. Nucl-ex/971208, 23 December 1997

[10] New results on low-mass lepton pair production in Pb-Au collisions at 158 GeV/c per nucleon; Proc. Int. Nuclear Physics Conf., Paris, August 1998, Nucl. Phys. A, to be published

[11] Heavy Ion Collisions at the LHC : the ALICE Experiment . by Loureno, C ; ALICE Collaboration. 1996 . . 31st Rencontre de Moriond : '96 QCD and High-energy Hadronic Interactions Les Arcs, France ; 23 - 30 Mar 1996 . Publ. in: Proceedings J Trn Thanh Vn Ed. Frontires, Gif-sur-Yvette, 1996 M93 (491-496

[12] J. Kapusta et al ,Phys. Rev. 2774 (1991)

[13] J. Rafelski, B. Muller, Phys. Rev. Lett. 48 (1982) 1066

J. Rafelski, B. Muller, Phys. Rev. Lett. 56 (1986) 2334

[14] J. Rafelski, Phys. Lett. B262 (1991) 333

[15] J. Rafelski, J Letessier, A. Tounsi, Hot hadronic matter and strange antibaryons, Phys. Lett. B292 (1992) 417-423

[16] M. Gadzinski, Strangeness and Pion production as signals of QCD phase International Symposium on Strangeness in Quark Matter : SQM '97 Thera, Santorini, Greece ; 14 - 18 Apr 1997 . Publ. in: Proceedings J. Phys., G : 23 (1997) 12 A D Panagiotou (1881-1888)

[17] Latessier, Tounsi, Heinz, Sollfrank, Strangeness conservation in hot hadronic fireballs, Physical rev. D, november 1992

[18] Latessier, Rafelski, Tounsi, Formation and evolution of quark-gluon plasma PAR/LPTHE/94-23, May 1994

[19] Diagnosis of QGP with strange hadrons Jan Rafelski and Jean Letessier Presented at the 29th Krakow school of theoretical physics, Zakopane, June 1999 (Acta physica polonica B 1999/2000)

[20] Λ, Ξ, Ω production in Pb-Pb and p-Pb interactions at 158 Gev/c, J.Phys. Nucl.Part.Phys. 25 (1998) 171.

[21] Andersen, E ; et al.,Enhancement of central Λ, Ξ and Ω yields in Pb-Pb collisions at 158 A GeV/c Phys. Lett., B : 433 (1998) 209

[22] J. Latessier, J. Rafelski, A. Tounsi, U. Heinz, J. Sollfrank Evidence for a high entropy phase in nuclear collisions, Phys. Rev. Letters 70 (1993) 3530-3533

[23] WA85 Collaboration: S. Abatzis et. al. Nucl. Phys. A590 (1995) 307c-315c

[24] WA94 Collaboration: S. Abatzis et. al. Nucl. Phys. A590 (1995) 317c-331c

[25] CERN Proposal SPSLC/P264: The NA49 experiment

[26] D. Kharzeev, C. Laurenco, M Nardi and H Satz, Zphys C74 (1997) 307 and references therein.

[27] Phys. Rev. , D-11 1975 3105: Production of hadrons at large m_T at 200,300 and 400 Gev

[28] Proposal: Study of baryon and antibaryon spectra in Lead-Lead interactions at 160 Gev/c per nucleon CERN/SPSLC 91-29 P263, 20 may 1991

[29] Paul Norman's midterm report, University of Birmingham, 1997

[30] Proposal: A search for centrally-produced non- $q\overline{q}$ mesons in proton-proton interactions at 450 Gev/c using the CERN Ω spectrometer and GAMS-400, CERN/SPSLC 94-22 pag 281, 15 August 1994

[31] Proposal: Study of strange and multi-strange particles in ultrarelativistic heavy ion collisions CERN/SP:SC/96-40 20 August 1996

[32] Handbook, National Bureau of Standards, procedure 25.5.20

[33] Review of Particle physics, European Physical Journal, C3 (1998)

[34] Gill P.E., Murray W. Minimization subject to bounds on the variables, National physical laboratory report NAC72,1976

[35] Strangeness enhancement at mid-rapidity in Pb-Pb collisions at 158 Gev/c WA97 collaboration, Journal of physics, Nucl. and part. phys 25 (1999) 181-188

[36] J. Podolanski and R. Armenteros: Phil Mag. 45 (1954) 13.

[37] P.I. Norman., thesis submitted to the university of Birmingham for the degree of Doctor of Philosophy, october 1999.

[38] P.I. Norman et al, Multi-strange particle production in p-Be, p-Pb and Pb-Pb collisions, Proceedings of XXXIIIth Rencontres de Moriond - QCD and High Energy Hadronic Interactions , 20-27 March 1999, Les Arcs 1800, France.